Eidgenössische Technische Hochschule Zürich
Swiss Federal Institute of Technology Zurich

Seminar for Applied Mathematics SAM

Asymptotic-Preserving Discretization of Three-Dimensional Plasma Fluid Models

T. Yu and R. Fuchs and R. Hiptmair

Research Report No. 2023-15

February 2023
Latest revision: March 2024

Seminar für Angewandte Mathematik
Eidgenössische Technische Hochschule
CH-8092 Zürich
Switzerland

Asymptotic-Preserving Discretization of Three-Dimensional Plasma Fluid Models

Tianwei Yu [*], Roman Fuchs [†], and Ralf Hiptmair [‡]

March 15, 2024

Abstract

We elaborate a numerical method for a three-dimensional hydrodynamic multi-species plasma model described by the Euler-Maxwell equations. Our method is inspired by and extends the one-dimensional scheme from [P. Degond, F. Deluzet, and D. Savelief, *Numerical approximation of the Euler-Maxwell model in the quasineutral limit*, Journal of Computational Physics, 231 (4), pp. 1917–1946, 2012]. It can cope with large variations of the Debye length λ_D and is robust in the quasi-neutral limit $\lambda_D \to 0$ thanks to its *asymptotic-preserving* (AP) property. The key ingredients of our approach are (i) a discretization of Maxwell's equations based on primal and dual meshes in the spirit of *discrete exterior calculus* (DEC) also known as the finite integration technique (FIT), (ii) a finite volume method (FVM) for the fluid equations on the dual mesh, (iii) *mixed implicit-explicit timestepping*, (iv) special no-flux and contact boundary conditions at an outer cut-off boundary, and (v) additional *stabilization* in the non-conducting region outside the plasma domain based on direct enforcement of Gauss' law. Numerical tests provide strong evidence confirming the AP property of the proposed method.

1 Introduction

The starting point for this work was the desire to numerically simulate the formation and evolution of electric arcs at atmospheric pressures. Following common practise, we rely on a mathematical description by means of a hydrodynamic multi-species plasma model, which boils down to an extended Maxwell-Euler system. The arc phenomenon covers a wide range of plasma regimes and, thus, the design goal was a numerical model capable of dealing with all of them seamlessly and simultaneously. Thus, in this work, as in [11], the focus is on *asymptotic-preserving* (AP) discretization in the quasi-neutral limit $\lambda \to 0$, where λ is the rescaled Debye length, see Sec. 2.2 for the underlying scaling arguments and [11, 9] for a discussion of the importance of the AP property of numerical plasma models.

Our approach is inspired by [11], but goes beyond that work in various directions:

- We supplement the Maxwell-Euler system by inter-species friction terms.
- We extend the spatially one-dimensional scheme of [11] to three spatial dimensions using discrete exterior calculus (DEC) to discretize Maxwell's equations combined with a low-order finite volume method for Euler's equations.
- We propose a stabilization in non-conducting regions which is essential for the efficacy of our method.

We stay close to [11] in terms of discretization in time employing semi-implicit time-stepping and base our illustration on the model situations shown in Fig. 1. Yet, we would like to remark that the mesh-based numerical scheme proposed in this paper can in principle be adapted to settings more general than those of Fig. 1. In particular, we do not assume any rotational symmetry, which would allow reduction to two spatial dimensions [35].

[*]Seminar for Applied Mathematics, ETH Zürich, tianwei.yu@math.ethz.ch
[†]IET Institut für Energietechnik, OST, roman.fuchs@ost.ch
[‡]Seminar for Applied Mathematics, ETH Zürich, ralf.hiptmair@math.ethz.ch

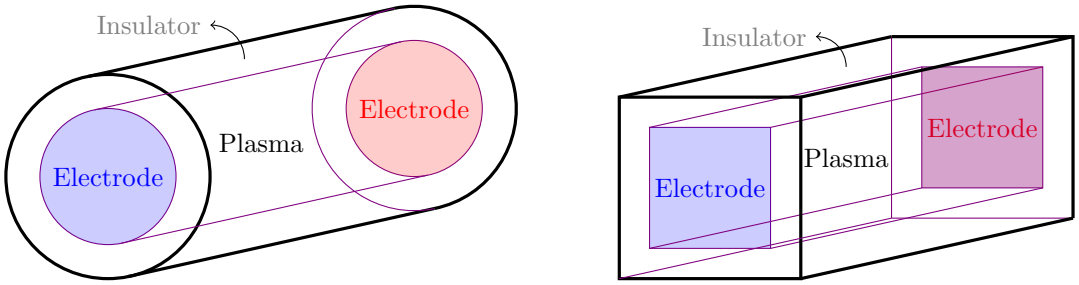

(a) Cylinder geometry **(b)** Cuboid geometry

Fig. 1. The special geometric setting suggested by the simulation of electric arcs, for which we discuss the new method.

The quasi-neutral limit of the Maxwell-Euler system leads to a singularly perturbed problem, that is, the limiting PDE system changes its type[1]. This poses a challenge for simulations in settings encompassing different regimes. Beside the quasi-neutral limit, we remind that singularly perturbed problems occur in extensively many physical models, e.g., in the case of vanishing viscosity problem [28, 3, 48], the zero-relaxation-limit of kinetic-type equations [43, 1], and the incompressible limit of compressible flows [29]. Throughout, it is essential that numerical schemes remain valid even if crucial model parameters approach the limit. These schemes are then said to be *asymptotic-preserving* (AP): Let us assume that we discretize a parameter (denoted by λ) dependent model P^λ, which converges to a limit P^0 as $\lambda \to 0$, by the scheme P_h^λ where h denotes some discretization parameter, e.g., the mesh size. The AP property amounts to uniform convergence of P_h^λ to the P^λ as $\lambda \to 0$. The concept is effectively depicted by a commuting diagram in [27, Fig. 1]. AP schemes have been extensively studied for various problems, e.g., the diffusive limit of kinetic equations [26, 34], the low Mach-number limit of compressible flow models [10, 19], magnetohydrodynamics [8], the quasi-neutral limit of drift-diffusion equations [2, 5]. For more information readers are referred to the comprehensive reviews [27, 9].

The content of this paper is organized as follows: In Sec. 2, we give a full description of the underlying equations of the Maxwell-Euler system and its rescaling procedure. Meanwhile, the boundary conditions in our setting is elaborated. A reformulation of Maxwell's equations in the non-conducting region is presented. Sec. 3 is devoted to the spatial discretization. The concept of primal-dual meshes is introduced based on which FIT and FVM are utilized. We discuss the full AP discretization in Sec. 4 and do numerical experiments in Sec. 5.

2 Plasma model

2.1 The Maxwell-Euler System

Plasmas consist of electrically charged and (possibly) neutral particle species, and we suppose that they can be treated as continua (fluids). That is, they may be described by the Navier-Stokes equations augmented with source terms for species generation (ionization, recombination), forces (Lorentz force and interspecies friction), and energy (thermal relaxation among species, radiative heat transfer, Ohmic heating). For more details on fluid models of plasmas, see [6, 45].

The electromagnetic effects in plasmas are governed by Maxwell's equations:

$$\partial_t \mathbf{B} + \nabla \times \mathbf{E} = 0, \tag{1a}$$
$$\partial_t \mathbf{D} - \nabla \times \mathbf{H} = -\mathbf{J}, \tag{1b}$$
$$\nabla \cdot \mathbf{B} = 0, \tag{1c}$$
$$\nabla \cdot \mathbf{D} = \rho, \tag{1d}$$

where the involved quantities[2] are the magnetic flux density $\mathbf{B}[\frac{\mathrm{Wb}}{\mathrm{m}^2}]$, the electric field $\mathbf{E}[\frac{\mathrm{V}}{\mathrm{m}}]$, the electric displacement field $\mathbf{D}[\frac{\mathrm{C}}{\mathrm{m}^2}]$, the magnetic field $\mathbf{H}[\frac{\mathrm{A}}{\mathrm{m}}]$, the electric current density $\mathbf{J}[\frac{\mathrm{A}}{\mathrm{m}^2}]$ and the electric charge

[1] The type of the Maxwell-Euler system switches from hyperbolic to mixed for $\lambda_D \to 0$

[2] SI units in square brackets.

density $\rho[\frac{\mathrm{C}}{\mathrm{m}^3}]$. These equations are known as Faraday's law (1a), Ampère's law (1b), Gauss's law for magnetism (1c) and Gauss's law for electric field (1d). For simplicity, we only consider isotropic and homogeneous media. Namely, we rely on linear constitutive relations (material laws):

$$\mathbf{D} = \epsilon \mathbf{E} \quad , \quad \mathbf{B} = \mu \mathbf{H}, \tag{2}$$

where $\epsilon[\frac{\mathrm{F}}{\mathrm{m}}]$ and $\mu[\frac{\mathrm{N}}{\mathrm{A}^2}]$ are the permittivity and permeability and assumed to be constant. By taking the time derivative of (1d) and the divergence of (1b), it is easy to see that (1b) and (1d) implies the charge conservation

$$\partial_t \rho + \nabla \cdot \mathbf{J} = 0. \tag{3}$$

Besides, by taking the divergence of equations (1a) and (1b) together with the relation (3), it is possible to verify that Gauss's laws (1c) (1d) are consequences of (1a) and (1b) provided that (1c) (1d) are satisfied at initial time. In other words, Gauss's laws (1c) (1d) can be thought of as initial conditions.

We model each species in the plasma as a compressible fluid through a set of *Euler equations* augmented by electromagnetic forces as well as other processes, e.g. collisions and recombination:

$$\partial_t \begin{pmatrix} n_* \\ m_* n_* \mathbf{u}_* \\ m_* n_* e_* \end{pmatrix} + \nabla \cdot \begin{pmatrix} n_* \mathbf{u}_* \\ m_* n_* \mathbf{u}_* \otimes \mathbf{u}_* + p_* \mathbb{I} \\ m_* n_* h_* \mathbf{u}_* \end{pmatrix} = \begin{pmatrix} 0 \\ q_* n_* (\mathbf{E} + \mathbf{u}_* \times \mathbf{B}) \\ \mathbf{J}_* \cdot \mathbf{E} \end{pmatrix} + \begin{pmatrix} \Gamma_* \\ \mathbf{R}_* \\ Q_* \end{pmatrix}. \tag{4}$$

The subscript $* \in \{e, i, \ldots\}$ labels electrons, ions or other species. The involved fluid quantities are: number density $n_*[\frac{1}{\mathrm{m}^3}]$, particle mass $m_*[\mathrm{kg}]$, electric charge $q_*[\mathrm{C}]$, velocity $\mathbf{u}_*[\frac{\mathrm{m}}{\mathrm{s}}]$, pressure $p_*[\frac{\mathrm{N}}{\mathrm{m}^2}]$, specific total energy $e_* := \frac{1}{2}|\mathbf{u}_*|^2 + \frac{p_*}{m_* n_* (\gamma - 1)}[\frac{\mathrm{J}}{\mathrm{kg}}]$, specific total enthalpy $h_* := e_* + \frac{p_*}{m_* n_*}[\frac{\mathrm{J}}{\mathrm{kg}}]$ and current density $\mathbf{J}_* := q_* n_* \mathbf{u}_*[\frac{\mathrm{A}}{\mathrm{m}^2}]$. All species are assumed to be ideal gases with heat capacity ratio $\gamma = 5/3$ for monatomic gases. The left-hand side of the equations describes the convection of plasma fluids. The first term at the right-hand side takes into account the Lorentz force in the momentum equation and Joule heating in the energy equation. $\Gamma_*, \mathbf{R}_*, Q_*$ are generic terms due to effects of inter-species collision, ionization, recombination, etc.

Combining the two sets of equations (1a) to (1d) and (4) leads to the governing equations for a multi-species plasma model. The coupling of the two subsystems is due to the fact that the flow of charged particles induces electric currents:

$$\rho = \sum_* q_* n_* \ , \quad \mathbf{J} = \sum_* q_* n_* \mathbf{u}_*. \tag{5}$$

Remark. *For the sake of simplicity, we only consider ion-electron collision in this work, but extension to more species is straightforward. Such collisions can be well modelled by friction terms, for instance [6, Sec. 5.6.2]*

$$\mathbf{R}_e^{coll} = \frac{\pi Z e^4 m_e^{1/2}}{(4\pi\epsilon)^2 (k_B T_e)^{3/2}} \ln\Lambda n_e n_i (\mathbf{u}_i - \mathbf{u}_e) = -\mathbf{R}_i^{coll}, \tag{6}$$

which is the collision force acting on electrons. $\ln\Lambda$ *is called the* Coulomb logarithm *and is usually taken as a constant [6]. Because of the conservation of momentum, the collision term for ions* $\mathbf{R}_i^{coll}$ *is nothing but the negative of* $\mathbf{R}_e^{coll}$*. In this work, the other effects, e.g. ionization and recombination, are not considered. For full details about the modeling of these physical processes, readers are referred to [15, Sec. 3.2].*

2.2 Rescaling

We arrive at non-dimensional equations by following the rescaling procedure of [9, Sec. 2.2]. First, a reference value for each quantity is fixed. We define $\overline{x}$ and $\overline{t}$ as space and time scale of interest, by which the reference velocity $\overline{v}$ is defined as $\overline{x}/\overline{t}$. The typical magnitudes of electromagnetic fields are $\overline{E}$ and $\overline{B}$. The reference magnitudes of fluid quantities are denoted by $\overline{u}$ for the plasma drift velocity, $\overline{n}$ for the plasma number density, $\overline{T}$ for the plasma temperature. On top of that, the reference pressure is set to $\overline{n} k_B \overline{T}$ with k_B being the Boltzmann constant; the reference value for the specific total energy and enthalpy is set to $\overline{u}^2$. Also taking into account the physical constants, i.e. the reference permittivity $\overline{\epsilon}$, the reference permeability $\overline{\mu}$, the light speed $c^2 = (\overline{\epsilon}\overline{\mu})^{-1}$, Boltzmann constant k_B, the elementary charge e, and ion mass m_i, we introduce the

following dimensionless parameters:

$$\xi := \frac{\overline{v}}{c} \text{ the velocity of interest } \textit{w.r.t.}^{1} \text{ the light speed},$$
$$\zeta := \frac{\overline{u}}{\overline{v}} \text{ the plasma velocity } \textit{w.r.t.} \text{ the speed of interest},$$
$$M := \frac{\overline{u}}{v_i^{\mathrm{th}}} \text{ the plasma drift velocity } \textit{w.r.t.} \text{ the thermal speed of ions, where } v_i^{\mathrm{th}} := \left(\frac{k_B\overline{T}}{m_i}\right)^{1/2},$$
$$\eta := \frac{e\overline{E}\overline{x}}{m_i\overline{u}^2} \text{ the electric energy } \textit{w.r.t.} \text{ the kinetic energy of ions},$$
$$\beta := \frac{\overline{v}\overline{B}}{\overline{E}} \text{ the induced electric field } \textit{w.r.t.} \text{ the total electric field},$$
$$\lambda := \frac{\lambda_D}{\overline{x}} \text{ the dimensionless Debye length, where } \lambda_D := \left(\frac{\epsilon k_B\overline{T}}{e^2\overline{n}}\right)^{1/2},$$
$$\varepsilon_*^2 := \frac{m_*}{m_i} \text{ the species mass } \textit{w.r.t.} \text{ the ion mass}, \quad * \in \{i, e, \ldots\},$$
$$g := \frac{1}{\overline{n}\lambda_D^3} \text{ the plasma parameter}^{2}.$$

Though rescaled, we keep the notations for the various quantities. We neglect ionization and recombination but retain collision terms, i.e. $\Gamma_* = 0, \mathbf{R}_* = \mathbf{R}_*^{\mathrm{coll}}, Q_* = Q_*^{\mathrm{coll}}$ in (4). The rescaled Euler-Maxwell system is

$$\beta\partial_t\mathbf{B} + \nabla\times\mathbf{E} = 0, \tag{7a}$$
$$\lambda^2\partial_t\mathbf{D} - \frac{\beta\lambda^2}{\xi^2}\nabla\times\mathbf{H} = -\frac{\zeta}{\eta M^2}\mathbf{J}, \tag{7b}$$
$$\nabla\cdot\mathbf{B} = 0, \tag{7c}$$
$$\lambda^2\eta M^2\nabla\cdot\mathbf{D} = \rho, \tag{7d}$$
$$\partial_t\begin{pmatrix} n_* \\ n_*\mathbf{u}_* \\ n_*e_* \end{pmatrix} + \nabla\cdot\begin{pmatrix} \zeta n_*\mathbf{u}_* \\ \zeta n_*\mathbf{u}_*\otimes\mathbf{u}_* + \zeta M^{-2}\varepsilon_*^{-2}p_*\mathbb{I} \\ \zeta n_*h_*\mathbf{u}_* \end{pmatrix} = \begin{pmatrix} 0 \\ \eta\zeta\varepsilon_*^{-2}q_*n_*\mathbf{E} + \eta\zeta^2\beta\varepsilon_*^{-2}q_*n_*\mathbf{u}_*\times\mathbf{B} \\ \zeta\eta\varepsilon_*^{-2}\mathbf{J}_*\cdot\mathbf{E} \end{pmatrix} + \begin{pmatrix} 0 \\ \varepsilon_*^{-2}\mathbf{R}_*^{\mathrm{coll}} \\ \varepsilon_*^{-2}Q_*^{\mathrm{coll}} \end{pmatrix}, \tag{7e}$$

where the equation of state becomes $e_* = \frac{1}{2}|\mathbf{u}_*|^2 + M^{-2}\frac{p_*}{\epsilon_*^2 n_*(\gamma-1)}$ and $h_* = e_* + M^{-2}\frac{p_*}{\epsilon_*^2 n_*}$. For a fully-ionized gas, we have the original expression of $\mathbf{R}_*^{\mathrm{coll}}$ in (6), and its rescaled expression becomes

$$\mathbf{R}_i^{\mathrm{coll}} = \frac{Z\ln\Lambda}{16\pi}g\lambda^{-1}M^{-1}\varepsilon_e n_e n_i(\mathbf{u}_i - \mathbf{u}_e). \tag{8}$$

Assumptions can be made to reduce the number of dimensionless parameters. Following [9, Sec. 2.2], the reference speed $\overline{v}$ is of the same scale as the plasma speed $\overline{u}$ and the thermal speed v_i^{th} whereas it is much smaller than the light speed c. Also, it is assumed that η and β are of order one and ξ has the same magnitude as λ.

Remark. *Special treatment is needed for the collision term. One could argue that the occurrence of λ^{-1} in (8) could lead to singular perturbation of the Euler system as $\lambda \to 0$. However, the validity of such a collision model is doubtful when $\lambda \to 0$. From the physical viewpoint, the shielding effect characterized by the rescaled Debye length λ limits the impact parameters to values $\sim \lambda$. The $\lambda \to 0$ limit implies that the collisions happen on the atomic length scale, in which quantum-mechanical effects must be taken into account [13, pp. 144-148]. Therefore, we eliminate the perturbation parameter in the friction term by assuming $g \sim \lambda$ and keep the prefactor α^{coll} of the collision term constant throughout the simulation.*

The case when there is an asymptotic parameter in the denominator of the friction term is of interest, too. This situation is known as relaxation limit, see [40, 50, 33, 7].

[1] Abbreviation of *with respect to*.

[2] It is basically the reciprocal of the number of particles per Debye sphere, see [16, Sec. 1.1]. Classical plasma theory assumes $g \ll 1$.

In summary, we make the following choices [9, sec 2.2]

$$\xi \sim g \sim \lambda \in [0,1], \quad \zeta \sim M \sim \eta \sim \beta \sim \mathcal{O}(1).$$

Assuming this behavior of the dimensionless parameters, the rescaled Euler-Maxwell system is simplified to a system of PDEs with the dimensionless *Debye length* λ as single parameter, whose value may tend to zero:

$$\partial_t \mathbf{B} + \nabla \times \mathbf{E} = 0, \tag{9a}$$

$$\lambda^2\, \partial_t \mathbf{D} - \nabla \times \mathbf{H} = -\mathbf{J}, \tag{9b}$$

$$\nabla \cdot \mathbf{B} = 0, \tag{9c}$$

$$\lambda^2\, \nabla \cdot \mathbf{D} = \rho, \tag{9d}$$

$$\partial_t \begin{pmatrix} n_* \\ n_* \mathbf{u}_* \\ n_* e_* \end{pmatrix} + \nabla \cdot \begin{pmatrix} n_* \mathbf{u}_* \\ n_* \mathbf{u}_* \otimes \mathbf{u}_* + \varepsilon_*^{-2} p_* \mathbb{I} \\ n_* h_* \mathbf{u}_* \end{pmatrix} = \begin{pmatrix} 0 \\ \varepsilon_*^{-2} q_* n_* (\mathbf{E} + \mathbf{u}_* \times \mathbf{B}) \\ \varepsilon_*^{-2} \mathbf{J}_* \cdot \mathbf{E} \end{pmatrix} + \begin{pmatrix} 0 \\ \varepsilon_*^{-2} \mathbf{R}_*^{\text{coll}} \\ \varepsilon_*^{-2} Q_*^{\text{coll}} \end{pmatrix}, \tag{9e}$$

with the equation of state $e_* = \frac{1}{2}|\mathbf{u}_*|^2 + \frac{p_*}{\varepsilon_*^2 n_* (\gamma - 1)}$ and $h_* = e_* + \frac{p_*}{\varepsilon_*^2 n_*}$. For a fully-ionized gas with only ions and electrons,

$$\mathbf{R}_i^{\text{coll}} = \alpha^{\text{coll}} n_e n_i (\mathbf{u}_i - \mathbf{u}_e) = -\mathbf{R}_e^{\text{coll}}, \tag{9f}$$

and consequently, the rescaled friction heat for ions and electrons takes the form:

$$Q_i^{\text{coll}} = \alpha^{\text{coll}} n_e n_i \mathbf{u}_i (\mathbf{u}_i - \mathbf{u}_e), \tag{9g}$$

$$Q_e^{\text{coll}} = \alpha^{\text{coll}} n_e n_i \mathbf{u}_e (\mathbf{u}_e - \mathbf{u}_i). \tag{9h}$$

The rescaled material laws (2) are still given by

$$\mathbf{D} = \epsilon \mathbf{E}, \quad \mathbf{B} = \mu \mathbf{H}, \tag{9i}$$

with rescaled permittivity ϵ and permeability μ, however. The λ-parameterized rescaled Maxwell-Euler system (9a)- (9i) is the starting point for the development of the numerical method.

Remark. *Structure preservation, that is, respecting inherent constraints satisfied by solution fields on the discrete level, is a major concern in discretization of (9) or related reduced models. Important constraints are the positivity of densities, entropy inequalities, and zero divergence of the* $\mathbf{B}$*-field. Two main approaches can be distinguished:*

(i) The first is to combine all equations into one hyperbolic system of conservation laws and apply finite volume methods. Such numerical methods are rather simple to implement and also computationally efficient. The challenge is to ensure the stability and the divergence constraint, which requires suitable numerical fluxes and limiters. Schemes that are provably positive, entropy-stable, or divergence-free have been constructed, see [53, 55, 54, 30, 14], and the references therein.

(ii) The second class of numerical methods tackles the electromagnetic and fluid subsystems separately. The rationale behind such a splitting strategy is that rather mature schemes for these parts are available. In particular, the divergence constraint can be easily handled by finite element exterior calculus. Yet the implementation of coupled solvers is usually complicated. To name some related work, [14] applies dedicated finite volume schemes to each subsystem; [25, 23] treat the electromagnetic part via finite element exterior calculus.

The scheme proposed in this work belongs to the second category and by construction satisfies the divergence-free constraint at the discrete level. Yet, our focus is on the AP property and not primarily on structure preservation.

2.3 Quasi-neutral Limit

The Debye length λ_D is the characteristic length over which the local net charge is shielded, see [6, Sec. 1.4] for the underlying physics. In many situations, it has a very small value compared to the reference length scale: the typical λ_D for gas discharge and Tokamak fusion reactors is 10^{-4} meter, for interstellar medium, the magnitude is about 1 meter [4, Chapt. 20]. Then the quasi-neutrality assumption $\rho = \sum_* q_* n_* \approx 0$ is justified, which is typical of the limit model. Formally we obtain it by setting the rescaled Debye length λ to zero in (9):

$$\begin{aligned} \partial_t \mathbf{B} + \nabla \times \mathbf{E} &= 0, && \text{(9a)} \\ \lambda^2 \partial_t \mathbf{D} - \nabla \times \mathbf{H} &= -\mathbf{J}, && \text{(9b)} \\ \nabla \cdot \mathbf{B} &= 0, && \text{(9c)} \\ \lambda^2 \nabla \cdot \mathbf{D} &= \rho. && \text{(9d)} \end{aligned} \quad \xrightarrow{\lambda \to 0} \quad \begin{aligned} \partial_t \mathbf{B} + \nabla \times \mathbf{E} &= 0, && \text{(10a)} \\ -\nabla \times \mathbf{H} &= -\mathbf{J}, && \text{(10b)} \\ \nabla \cdot \mathbf{B} &= 0, && \text{(10c)} \\ 0 &= \rho. && \text{(10d)} \end{aligned}$$

The quasi-neutrality condition (10d) is the consequence of setting $\lambda = 0$ in Gauss's law for the electric field (9d). As in the non-neutral case, Gauss's laws (10c) (10d) are the consequence of (10a) (10b) provided (10c) (10d) are satisfied at initial time.

Remark. *The limit* (10) *represents a* singular perturbation problem *in the sense that vanishing λ changes the character of the PDE system. To be more specific, for $\lambda = \mathcal{O}(1)$ the* **E***-field evolves with time whereas in the quasi-neutral model, it responds instantaneously to other quantities according to the constraint (10b). We replace (9b) by the sum of the rotation of (9a) and the time-derivative of (9b). Meanwhile, due to the link between fluid momenta $n_* u_*$ and current in (5), the term $\partial_t \mathbf{J}$ can be reformulated by the momentum equation according to (9e) and we end up with the following wave equation with the source terms:*

$$\lambda^2 \partial_t^2 \mathbf{E} + \nabla \times \nabla \times \mathbf{E} = \mathbf{S}_1 + \mathbf{S}_2, \tag{11}$$

where

$$\mathbf{S}_1 = -\left(\sum_* \varepsilon_*^{-2} q_*^2 n_* \right) \mathbf{E}, \tag{12}$$

$$\mathbf{S}_2 = \sum_* q_* \nabla \cdot (n_* \mathbf{u}_* \otimes \mathbf{u}_* - \varepsilon_*^{-2} p_* \mathbb{I} \varepsilon_*^{-2} q_*^2 n_* \mathbf{u}_* \times \mathbf{B} - q_* \varepsilon_*^{-2} \mathbf{R}_*^{coll}). \tag{13}$$

It is obvious in (11) that the electric field propagates with finite speed (hyperbolic evolution) when $\lambda = \mathcal{O}(1)$, whereas for $\lambda = 0$ it responds instantaneously everywhere to local excitation (parabolic evolution/elliptic boundary value problems).

Remark. *The preceding formal limit argument is heuristic. Deep mathematical tools from perturbation theory would be needed to rigorously prove the convergence of the limiting sequence. This topic is beyond the scope of this paper. Readers are referred to [45, Chapt. 2] [39] for the quasi-neutral limit of the Maxwell-Euler system and [24, 20] for some general theory.*

2.4 Boundary Conditions

We consider a simply-connected domain Ω comprising two subdomains Ω_P (**p**lasma domain) and Ω_N (**n**on-conducting domain). They represent regions of space occupied by plasma and a non-conducting linear dielectric medium (e.g. glass) respectively. We use the notation $\Gamma_C := \partial\Omega \cap \partial\Omega_P$ to denote the contact boundary, and $\Gamma_I := \partial\Omega \cap \partial\Omega_N$ for the insulating boundary which is an "artificial" cut-off boundary. The interface between the two domains is denoted by $\Gamma_W = \partial\Omega_I \cap \partial\Omega_P$. A geometric arrangement corresponding to this setting is sketched in Fig. 2 and is the one used in [15, Chapt. 1, Sec. 4]. This situation is simple but highly relevant. It covers fundamental experimental set-ups, for example, those studying wall-stabilized electric arcs [17], but is also adequate for a range of industrial plasmas, for instance, for those occurring in high-voltage circuit breakers [44, 37].

The Euler equations are defined in Ω_P with boundary conditions on $\partial\Omega_P$. We consider the physical scenario where the plasma is confined by a solid insulator. Therefore, the interface Γ_W is treated as a reflective wall where fluid particles are bouncing back while keeping the tangential velocity and energy unchanged. The contact boundary Γ_C is modelled by open boundaries, where charge carriers and energy can pass through, i.e., ions and electrons are emitted and absorbed by the electrodes.

Remark. *The treatment of electrodes as open boundary is a simplification. For more realistic electrode modelling, see [18, 38].*

Maxwell's equations are posed on the whole domain Ω. The insulating boundary Γ_I blocks energy transfer and therefore only admits zero electric and magnetic flux, that is, $\mathbf{D} \cdot \mathbf{n}|_{\Gamma_I} = 0$ and $\mathbf{B} \cdot \mathbf{n}|_{\Gamma_I} = 0$ where $\mathbf{n}$ is the normal vector [22]. We model the electrodes by imposing boundary conditions on the contact boundary

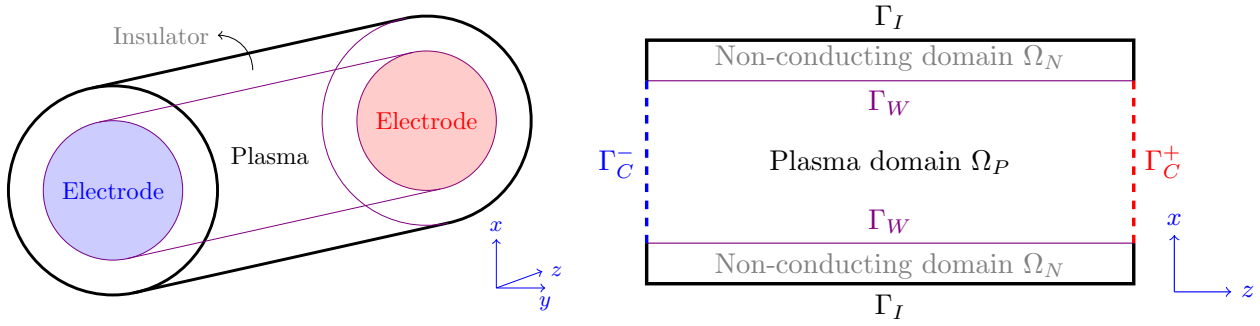

Fig. 2. The right figure shows the cross section in the x-z plane and the different parts of the boundary and interfaces.

$\Gamma_C = \Gamma_C^+ \cup \Gamma_C^-$, which is composed of two disjoint connected components. On the contact boundary Γ_C, the tangential component $\mathbf{E}_t$ of the $\mathbf{E}$-field vanishes. By Faraday's law (9a) we have $\nabla \times \mathbf{E} \cdot \mathbf{n} = 0$ on the whole (topologically trivial) boundary $\partial\Omega$, which admits a scalar potential φ defined on $\partial\Omega$ such that $\mathbf{E}_t = \nabla_\Gamma \varphi$ where ∇_Γ denotes surface gradient. The scalar potential φ is constant on Γ_C^+ and Γ_C^-. The difference of these two constant values gives the voltage drop between the two contacts. We summarize the boundary conditions for both sets of equations:

For the Euler equations:

$$\begin{aligned} \mathbf{u}_* \cdot \mathbf{n} &= 0 \quad \text{on} \quad \Gamma_W, \\ \nabla \mathbf{u}_* \cdot \mathbf{n} &= \mathbf{0} \quad \text{on} \quad \Gamma_C, \\ \nabla n_* \cdot \mathbf{n} &= 0 \quad \text{on} \quad \Gamma_W \cup \Gamma_C, \\ \nabla e_* \cdot \mathbf{n} &= 0 \quad \text{on} \quad \Gamma_W \cup \Gamma_C. \end{aligned}$$

For Maxwell's equations:

$$\begin{aligned} \mathbf{D} \cdot \mathbf{n} &= 0 \quad \text{on} \quad \partial\Omega, \\ \mathbf{B} \cdot \mathbf{n} &= 0 \quad \text{on} \quad \Gamma_I, \\ \varphi &= \varphi^{\pm}(t) \quad \text{on} \quad \Gamma_C^{\pm}. \end{aligned}$$

Remark. *No interface condition for Maxwell's equations is needed on* Γ_W.

Remark. *For a geometric setting with non-trivial topology, e.g. with a tunnel,* $\nabla \times \mathbf{E} \cdot \mathbf{n} = 0$ *does not guarantee the existence of a surface potential* φ *satisfying* $\mathbf{E}_t = \nabla_\Gamma \varphi$. *One needs to include co-homology vector fields [22].*

2.5 Stabilization in Ω_N

No plasma fills the non-conducting domain Ω_N (see Fig. 2), and, consequently, the Maxwell system in Ω_N reduces to

$$\partial_t \mathbf{B} + \nabla \times \mathbf{E} = 0, \tag{14a}$$
$$\lambda^2 \partial_t \mathbf{D} - \nabla \times \mathbf{H} = 0, \tag{14b}$$
$$\nabla \cdot \mathbf{B} = 0, \tag{14c}$$
$$\lambda^2 \nabla \cdot \mathbf{D} = 0. \tag{14d}$$

In a non-neutral regime where $\lambda = \mathcal{O}(1)$, the Maxwell system in Ω_N is well-posed and Gauss's laws (14c) (14d) are redundant as long as they are satisfied at initial time. Nonetheless, as the system approaches the quasi-neutral limit as $\lambda \to 0$, Gauss's law for the $\mathbf{D}$-field (14d) is no longer enforced. Schemes based on this set of PDEs would become unstable as $\lambda \to 0$. The vanishing divergence constraint would evaporate as $\nabla \cdot \mathbf{D} = 0/\lambda^2 = 0$ would not hold numerically when λ^2 becomes extremely small.

To view this issue from another perspective, we examine the limit Maxwell system in Ω_N:

$$\partial_t \mathbf{B} + \nabla \times \mathbf{E} = 0, \tag{15a}$$
$$-\nabla \times \mathbf{H} = 0, \tag{15b}$$
$$\nabla \cdot \mathbf{B} = 0, \tag{15c}$$
$$\nabla \cdot \mathbf{D} = 0. \tag{15d}$$

Again, Gauss's law for the **B**-field (15c) is redundant, while Gauss's law for the **D**-field (15d) is no longer a consequence of Ampère's law (15b). However, (15d) is essential for the well-posedness of the problem [42, p. 7]. Obviously, the degeneracy of Gauss's law for the **D**-field in the system (15a) to (15d) as $\lambda \to 0$ poses some problem. In other words, the set of equations (15a) to (15d) switches to an ill-posed situation for $\lambda = 0$. I computations this will manifest itself as instability already for $\lambda > 0$.

As a remedy, we propose the following reformulation which introduces a scalar Lagrange multiplier ψ and removes the λ^2 prefactor in Gauss's law for the **D**-field:

$$\partial_t \mathbf{B} + \nabla \times \mathbf{E} = 0, \tag{16a}$$

$$\lambda^2 \partial_t \mathbf{D} - \nabla \times \mathbf{H} + \nabla\psi = 0, \tag{16b}$$

$$\nabla \cdot \mathbf{B} = 0, \tag{16c}$$

$$\nabla \cdot \mathbf{D} = 0. \tag{16d}$$

Supplemented with the boundary condition $\psi = 0$ on $\partial\Omega_N$, one can check that (16a) to (16d) are equivalent to the original formulation (14a)-(14d) by verifying that $\psi = 0$ in Ω_N. This is done by taking the divergence of (16b), which results in $\Delta\psi = 0$ and the zero Dirichlet boundary condition gives vanishing ψ. The importance of this reformulation will become clear through numerical experiments, see Sec. 5.

We point out that this reformulation is not needed in the plasma domain Ω_P since the Maxwell system is uniformly well-posed for $\lambda \in [0, 1]$ thanks to the existence of an electric current and its dependence on the **E**-field.

3 Spatial Discretization

3.1 Primal-dual Staggered Meshes

3.1.1 Definition and Geometric Construction

To prepare the spatial discretization of the Maxwell-Euler system, we introduce primal-dual staggered meshes, a key component of the discrete exterior calculus (DEC) discretization of Maxwell's equations. The spatial domain is covered by two meshes interlacing with each other, denoted by a mesh doublet $(\mathcal{M}, \tilde{\mathcal{M}})$ for primal mesh and dual mesh respectively. The fundamental duality property requires that *each edge of one mesh penetrates a face of the other mesh and that each vertex of one mesh lies inside of a cell of the other mesh* [52, Sec. 2]. Examples are shown in Fig. 3a.

To clarify the notation, in three dimensions the primal mesh $\mathcal{M}$ is a cell complex defined by the set of mesh entities $\{P, L, A, V\}$[3] denoting *vertices (points), edges, faces* and *cells* respectively. In the same way, the dual mesh $\tilde{\mathcal{M}}$ is defined by $\{\tilde{P}, \tilde{L}, \tilde{A}, \tilde{V}\}$. The entities of two meshes are connected by one-on-one pairings $P \leftrightarrow \tilde{V}$, $L \leftrightarrow \tilde{A}$, $A \leftrightarrow \tilde{L}$ and $V \leftrightarrow \tilde{P}$, which arise in a very natural way: $P(\tilde{P}$ resp.,) corresponds to $\tilde{V}(V$ resp.,) in which it lies and $L(\tilde{L}$ resp.,) penetrates a corresponding $\tilde{A}(A$ resp.,). According to their dimensions, vertices, edges, faces and cells are also called 0-dim, 1-dim, 2-dim and 3-dim entities respectively. Moreover, we denote by $N_*, * \in \{P, \tilde{P}, L, \tilde{L}, A, \tilde{A}, V, \tilde{V}\}$ the total number of entities in $\mathcal{M}, \tilde{\mathcal{M}}$.

In 2D we construct the pair of meshes based on the Delaunay-Voronoi approach: we start with a Delaunay triangulation $\mathcal{M}$ of the domain and construct $\tilde{\mathcal{M}}$ by connecting *circumcenters* of any two adjacent triangles, see Fig. 3b. In three dimensions, the meshes are constructed by extruding the 2D meshes vertically along one axis in a staggered manner [36, Sec. 3.1]. See an example in Fig. 3c. In this way, the meshes are composed of prisms. This particular choice is compatible with the cylindrical geometric setting that we are in, see Fig. 2. For a general setting, one can directly decompose the domain into tetrahedrons and constructs the Voronoi grid, but the procedure is more complicated. The meshes for the cylindrical domain are displayed in Fig. 5a.

The geometric orthogonality between $L \leftrightarrow \tilde{A}$ and $A \leftrightarrow \tilde{L}$ is satisfied and will be a crucial property for approximating the material laws on the discrete level (which is the so-called discrete Hodge operator [21, 46]), as will be shown in Sec. 3.2.1.

Remark. *The use of the Delaunay-Voronoi based primal-dual meshes is problematic when there are triangles with an obtuse angle in $\mathcal{M}$. In this case their circumcenters lie outside the triangles and the intersection between edges and faces is violated. An alternative approach is barycenter-based dual meshes, which are not restricted to an acute-angle triangulation [36, Sec. 4.2].*

[3] The notation here is a bit sloppy. P, L, A, V can refer to a single entity or a set of entities depending on the context.

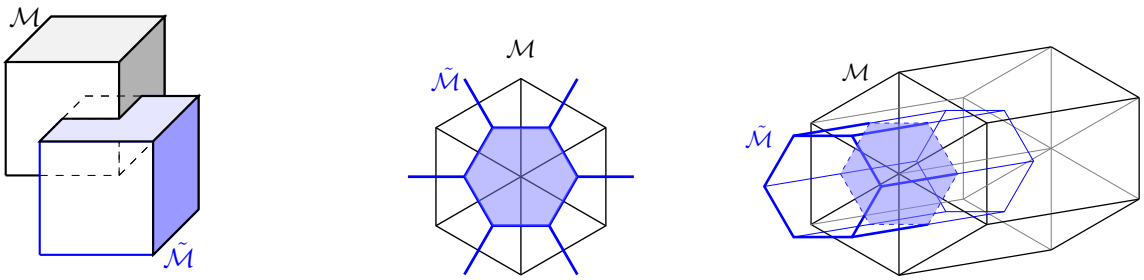

(a) 3D case (Cartesian) **(b)** 2D case **(c)** 3D case (2D extrusion)

Fig. 3. Illustration of primal and dual meshes. **(a)** A Cartesian case ("staggered grids") **(a)** A Delaunay-Voronoi grid in 2D **(c)** The extrusion of 2D mesh: six triangular prisms are primal cells (with black and gray edges). One dual cell, which is a hexagonal prism, is depicted by blue edges. The dashed hexagon represents the intersection of the dual cell and primal cells.

3.1.2 Orientation and Incidence Matrices

Each geometric entity in the primal mesh $\mathcal{M}$ is (arbitrarily) endowed with an *internal orientation*[4]. The notion is illustrated in Fig. 4. For the entities of the dual mesh $\tilde{\mathcal{M}}$, we set their internal orientations to be aligned with their corresponding primal entities according to the bijective pairings, i.e. edges penetrate faces.

Another orientation attribute, *induced orientation*, is defined as follows: an induced orientation of a k-dim entity f with respect to a $(k+1)$-dim entity f', satisfying $f \subset \partial f'$, is determined by the internal orientation of f' according to the rules shown in Fig. 4.

This information can be described by matrices with entries in $\{0, -1, +1\}$, called *incidence matrices*. To describe the primal face-to-edge relation, for instance, a sparse matrix $\mathbb{C} \in \mathbb{R}^{N_A \times N_L}$ is assembled whose (i, j)-entry is assigned $+1$ if the internal orientation of edge L_j and its induced orientation with respect to face A_i coincides; it is assigned -1 if two orientations are opposite; and assigned 0 if L_j is not a subset of the boundary of A_i. We will see later that $\mathbb{C}$ functions as a discrete version of the rotation operator. The other incidence matrices are constructed in the same manner, see Tab. 1 for a summary. Given the relationship of orientations of $\mathcal{M}$ and $\tilde{\mathcal{M}}$, we can derive the relations listed in Tab. 2.

Matrix	Size	Incidence relation	Operator
$\mathbb{D}$ $(\tilde{\mathbb{D}})$	$N_V \times N_A$ $(N_{\tilde{V}} \times N_{\tilde{A}})$	cell $\rightarrow$ face	discrete divergence
$\mathbb{C}$ $(\tilde{\mathbb{C}})$	$N_A \times N_L$ $(N_{\tilde{A}} \times N_{\tilde{L}})$	face $\rightarrow$ edge	discrete rotation
$\mathbb{G}$ $(\tilde{\mathbb{G}})$	$N_L \times N_P$ $(N_{\tilde{L}} \times N_{\tilde{P}})$	edge $\rightarrow$ vertex	discrete gradient

Tab. 1. Summary of incidence matrices

Property of incidence matrices	Corresponding rule in vector analysis
$\mathbb{G}^T = -\tilde{\mathbb{D}}$	$\nabla^* = -(\nabla\cdot)$
$\mathbb{C}^T = \tilde{\mathbb{C}}$	$(\nabla\times)^* = (\nabla\times)$
$\mathbb{D}^T = -\tilde{\mathbb{G}}$	$(\nabla\cdot)^* = -\nabla$
$\mathbb{C}\mathbb{G} = \mathbf{0}, \tilde{\mathbb{C}}\tilde{\mathbb{G}} = \mathbf{0}$	$(\nabla\times) \circ \nabla = 0$
$\mathbb{D}\mathbb{C} = \mathbf{0}, \tilde{\mathbb{D}}\tilde{\mathbb{C}} = \mathbf{0}$	$(\nabla\cdot) \circ (\nabla\times) = 0$

$*$ denotes adjoint operator.

Tab. 2. Relations between incidence matrices

These matrices are topological and thus invariant under smooth deformation of the domain. In the next section, we will show that they play a crucial role in constructing discrete Maxwell's equations.

[4]This notion should not be confused with *inner orientation*, which has a slightly different definition, see [49, Sec. 3.1].

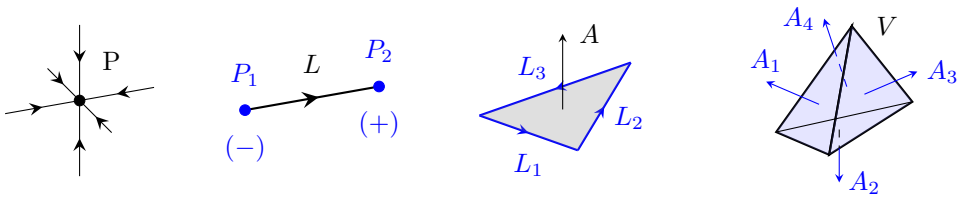

Fig. 4. Illustration of internal and induced orientations. The internal orientation of each entity is depicted in black: vertices are oriented as *sink* by default; edges are oriented by their pointing direction; faces are oriented by their normal vector; cells are oriented positive by default. The induced orientations are depicted in blue: the ending vertex of an edge is negatively oriented while the starting point is positively oriented; the orientations of edges with respect to a face obey the right-hand rule; a face of a cell are oriented by its outer normal vector.

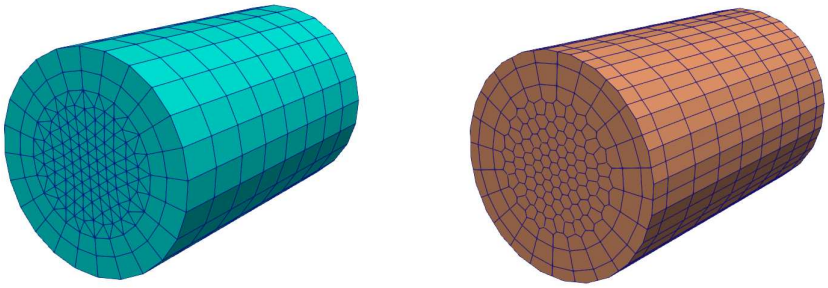

(a) Cylinder geometry

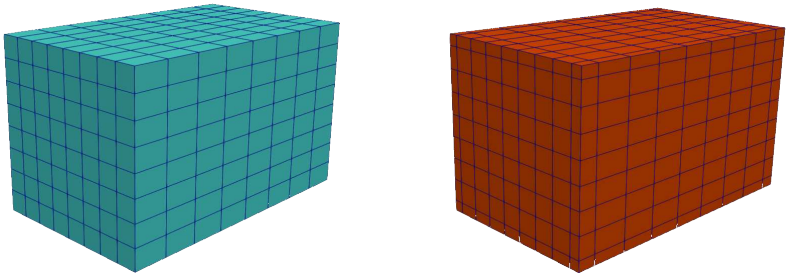

(b) Cuboid geometry

Fig. 5. Examples of primal (left) and dual meshes (right)

3.1.3 Cut-off Boundary

The primal mesh $\mathcal{M}$ is generated first and resolves the domain boundary $\partial\Omega$. The dual mesh $\tilde{\mathcal{M}}$ is generated afterwards. To make both meshes aligned at the boundary, we have to truncate the *dual* entities near the boundary. In addition, auxiliary geometric entities are needed to close $\tilde{\mathcal{M}}$, see Fig. 6.

Note that the auxiliary edges might not be straight and the auxiliary faces might not be flat as is shown in Fig. 6, which necessitates a versatile data structure to include such situations. In the following, the auxiliary entities will be treated as dual entities, which limits the validity of the relations in Tab. 2 to the interior part of $\tilde{\mathcal{M}}$. For a more systematic illustration that considers the boundary dual entities, see [21, Sec. 5]. A pair of primal and dual meshes for the geometry in Fig. 2 is displayed in Fig. 5a.

3.2 Discrete Maxwell Equations

3.2.1 Finite Integration Technique (FIT)

We utilize FIT to discretize Maxwell's equations. This framework was originally proposed in [51] and can be regarded as a generalization of Yee's FDTD method [56]. To derive a discrete model for the (rescaled) Maxwell

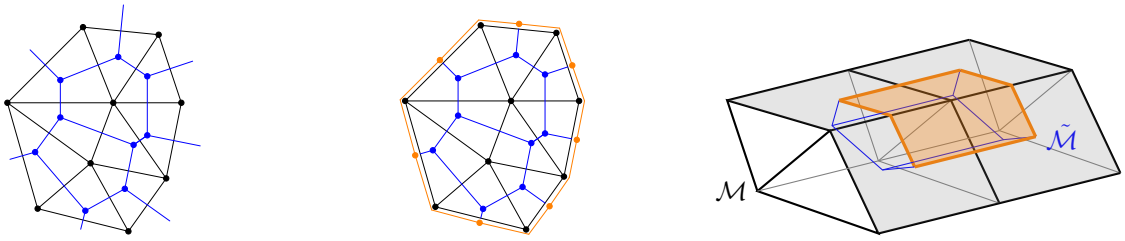

(a) Before cut-off **(b)** After cut-off **(c)** 3D case

Fig. 6. Illustration of cut-off boundary. Before the cut-off, the boundary of $\tilde{\mathcal{M}}$ is not well-defined. To resolve the same boundary as $\mathcal{M}$, boundary dual cells are truncated and auxiliary entities are supplemented (shown in orange color). To be specific, in subfigure (c) four edges and one face are added in order to close this dual cell. Notice that these auxiliary edges and faces can be non-straight and non-flat.

equations (9a)-(9d), we first cast them into integral form:

$$\oint_{\partial A} \mathbf{E}\cdot \mathrm{d}\mathbf{s} \;= -\iint_{A} \partial_t \mathbf{B}\cdot \mathrm{d}\mathbf{A}, \tag{17a}$$

$$\oint_{\partial A} \mathbf{H}\cdot \mathrm{d}\mathbf{s} \;= \iint_{A} \left(\lambda^2\partial_t \mathbf{D}+\mathbf{J}\right)\cdot \mathrm{d}\mathbf{A}, \tag{17b}$$

$$\oint_{\partial V} \mathbf{B}\cdot \mathrm{d}\mathbf{A} = 0, \tag{17c}$$

$$\oint_{\partial V} \lambda^2\mathbf{D}\cdot \mathrm{d}\mathbf{A} = \iiint_{V} \rho \mathrm{d}V. \tag{17d}$$

where A, V stand for arbitrary surfaces and cells in the spatial domain.

Given the mesh pair $(\mathcal{M}, \tilde{\mathcal{M}})$, the discrete Maxwell system arises from restricting the integrals (17a)-(17d) to the entities in $(\mathcal{M}, \tilde{\mathcal{M}})$. We end up with

$$\sum_{k:L_k\in\partial A_l} \underbrace{\int_{L_k} \mathbf{E}\cdot \mathrm{d}\mathbf{s}}_{:=e_k} = -\partial_t \underbrace{\iint_{A_l} \mathbf{B}\cdot \mathrm{d}\mathbf{A}}_{:=b_l}, \qquad l=1,...,N_A, \tag{18a}$$

$$\sum_{k:\tilde{L}_k\in\partial \tilde{A}_l} \underbrace{\int_{\tilde{L}_k} \mathbf{H}\cdot \mathrm{d}\mathbf{s}}_{:=h_k} = \lambda^2\partial_t \underbrace{\iint_{\tilde{A}_l} \mathbf{D}\cdot \mathrm{d}\mathbf{A}}_{:=d_l} + \underbrace{\iint_{\tilde{A}_l} \mathbf{J}\cdot \mathrm{d}\mathbf{A}}_{:=j_l}, \qquad l=1,...,N_{\tilde{A}}, \tag{18b}$$

$$\sum_{k:A_k\in\partial V_l} \iint_{A_k} \mathbf{B}\cdot \mathrm{d}\mathbf{A} = 0, \qquad l=1,...,N_V, \tag{18c}$$

$$\lambda^2 \sum_{k:\tilde{A}_k\in\partial \tilde{V}_l} \iint_{\tilde{A}_k} \mathbf{D}\cdot \mathrm{d}\mathbf{A} = \underbrace{\iiint_{\tilde{V}_l} \rho \mathrm{d}V}_{:=q_l}, \qquad l=1,...,N_{\tilde{V}}. \tag{18d}$$

where k, l number the entities in $(\mathcal{M}, \tilde{\mathcal{M}})$. The integral field quantities are the unknowns of the discrete Maxwell model. As is defined in (18a)-(18d) by the underbraces, these unknowns are stacked into vectors:

$$\mathbf{e} := \{e_k\}_{k=1}^{N_L},\quad \mathbf{b} := \{b_k\}_{k=1}^{N_A},\quad \mathbf{h} := \{h_k\}_{k=1}^{N_{\tilde{L}}},\quad \mathbf{d} := \{d_k\}_{k=1}^{N_{\tilde{A}}},\quad \mathbf{j} := \{j_k\}_{k=1}^{N_{\tilde{A}}},\quad \mathbf{q} := \{q_k\}_{i=k}^{N_{\tilde{V}}}. \tag{19}$$

Remark. *In an implementation, it is always convenient to index a pair of corresponding primal and dual entities with the same number. For instance, a primal face A_k is penetrated by the dual edge $\tilde{L}_k$. In the following discussion, we stick to this convention, which will simplify our notation.*

The material laws (2) need to be taken into account within this framework, that is, relations $\mathbf{b} = \mathbb{M}_\mu \mathbf{h}$ and $\mathbf{d} = \mathbb{M}_\epsilon \mathbf{e}$ with suitable *material* matrices $\mathbb{M}_\mu, \mathbb{M}_\epsilon$. When the orthogonality of the pair $(\mathcal{M}, \tilde{\mathcal{M}})$ holds, the discrete material laws can consistently be represented by *diagonal matrices* with entries

$$(\mathbb{M}_\mu)_{k,k} = \frac{\mu|A_k|}{|\tilde{L}_k|}, \qquad (\mathbb{M}_\epsilon)_{k,k} = \frac{\epsilon|\tilde{A}_k|}{|L_k|},$$

where $|\cdot|$ denotes taking length or area. We would like to remark that an approximation error is introduced due to the implicit assumption that vector fields are piecewise constant, see the analysis in [36, Sec. 3.2].

With the aid of incidence matrices defined in the preceding section and given the discrete material law, (18a)-(18d) can be recast into a set of algebraic equations:

$$\begin{aligned} \partial_t \mathbf{B} + \nabla \times \mathbf{E} &= 0, \\ \lambda^2 \partial_t \mathbf{D} - \nabla \times \mathbf{H} &= -\mathbf{J}, \\ \nabla \cdot \mathbf{B} &= 0, \\ \lambda^2 \nabla \cdot \mathbf{D} &= \rho, \\ \mathbf{H} &= \mu^{-1}\mathbf{B}, \\ \mathbf{D} &= \epsilon \mathbf{E}. \end{aligned} \quad \xrightarrow{(\mathcal{M}, \tilde{\mathcal{M}})} \quad \begin{aligned} \dot{\mathbf{b}} + \mathbb{C}\mathbf{e} &= \mathbf{0}, && \text{(20a)} \\ \lambda^2 \dot{\mathbf{d}} - \tilde{\mathbb{C}}\mathbf{h} &= -\mathbf{j}, && \text{(20b)} \\ \mathbb{D}\mathbf{b} &= \mathbf{0}, && \text{(20c)} \\ \lambda^2 \tilde{\mathbb{D}}\mathbf{d} &= \mathbf{q}, && \text{(20d)} \\ \mathbf{h} &= \mathbb{M}_\mu^{-1}\mathbf{b}, && \text{(20e)} \\ \mathbf{d} &= \mathbb{M}_\epsilon \mathbf{e}, && \text{(20f)} \end{aligned}$$

where the dot on top of quantities stands for the time derivative.

Remark. *At this point, we would like to emphasize the importance of the primal-dual staggered meshes:* the material laws can be included in a rather simple way. *For Gauss's law* $\mathbf{D} = \epsilon\mathbf{E}$*, for instance, the* $\mathbf{D}$*-field is represented by a collection of face integrals* $\{d_k\}_k$ *while the* $\mathbf{E}$*-field is represented by a collection of edge integrals* $\{e_k\}_k$*. The primal-dual meshes allow us to arrange them in a staggered way – edges penetrate faces – such that* $\mathbf{D} = \epsilon\mathbf{E}$ *can be approximated by* $\mathbf{d} = \mathbb{M}_\epsilon \mathbf{e}$ *in a local fashion, i.e.* $\mathbb{M}_\epsilon$ *is diagonal. A more schematic illustration relies on the language of discrete exterior calculus (DEC), see [46, 47, 21].*

Summing up, the essence of DEC/FIT is the following:

(i) The discrete Maxwell model (20a)-(20d) are topological in the sense that they are invariant under different coordinate systems. Only the discrete material laws (20e)(20e) depend on the geometric information.

(ii) The discrete Maxwell model (20a)-(20d) is free of approximation error, that is, it holds for exact fields. A consistency error is introduced only by the discrete material laws (20e)(20e).

3.2.2 Discrete Boundary Conditions

The electromagnetic boundary $\partial\Omega = \Gamma_C \cup \Gamma_I$ is resolved by the primal mesh $\mathcal{M}$. As is mentioned in Sec. 2.4, the zero-magnetic-flux boundary condition $\mathbf{B}\cdot\mathbf{n}$ is equivalent to $(\nabla \times \mathbf{E})\cdot\mathbf{n} = 0$, which paves the way for a surface scalar potential $\varphi : \partial\Omega \to \mathbb{R}$ such that the tangential component $\mathbf{E}_t$ of the $\mathbf{E}$-field is equal to $\nabla_\Gamma \varphi$. This remains true on the discrete level. We associate with each primal vertex $P_k \in \partial\Omega$ a scalar value φ_k. Therefore, the boundary conditions (see Sec. 2.4) are discretized in the following way:

$$\begin{aligned} \mathbf{D}\cdot\mathbf{n} = 0 \quad &\text{on} \quad \Gamma_I, \\ \mathbf{B}\cdot\mathbf{n} = 0 \quad &\text{on} \quad \Gamma_I, \\ \varphi = \varphi^{\pm}(t) \quad &\text{on} \quad \Gamma_C^{\pm}, \end{aligned} \quad \xrightarrow{(\mathcal{M}, \tilde{\mathcal{M}})} \quad \begin{aligned} d_k = 0, \ \ &\forall k : \tilde{A}_k \subset \Gamma_I, && \text{(21a)} \\ e_k = (\mathbb{G}\mathbb{X}_\varphi \boldsymbol{\varphi})_k, \ \ &\forall k : L_k \subset \partial\Omega, && \text{(21b)} \\ \varphi_k = \varphi^{\pm}(t), \ \ &\forall k : P_k \subset \Gamma_C^{\pm}, && \text{(21c)} \end{aligned}$$

where $\mathbb{X}_\varphi \in \mathbb{R}^{N_P \times N_P^\partial}$ extends $\boldsymbol{\varphi}$ to all the primal vertices by zero. Obviously, the surface gradient ∇_Γ is represented by $\mathbb{G}\mathbb{X}_\varphi$.

3.2.3 Stabilization in Ω_N

In Sec. 2.5, we have proposed a stabilization of the Maxwell system in the non-conducting domain Ω_N by introducing a Lagrange multiplier. On the semi-discrete level, the equations to be solved in Ω_N are

$$\begin{aligned} \partial_t \mathbf{B} + \nabla \times \mathbf{E} &= 0, \\ \lambda^2 \partial_t \mathbf{D} - \nabla \times \mathbf{H} + \nabla\psi &= 0, \\ \nabla \cdot \mathbf{D} &= 0. \end{aligned} \quad \xrightarrow{(\mathcal{M}, \tilde{\mathcal{M}})} \quad \begin{aligned} [\dot{\mathbf{b}} + \mathbb{C}\mathbf{e} = \mathbf{0}]_k, \ \ &\forall k : A_k \subset \Omega_N, && \text{(22a)} \\ [\lambda^2 \dot{\mathbf{d}} - \tilde{\mathbb{C}}\mathbf{h} + \mathbb{H}\mathbb{G}\mathbb{X}_\psi \boldsymbol{\psi} = \mathbf{0}]_k, \ \ &\forall k : \tilde{A}_k \subset \Omega_N && \text{(22b)} \\ [\tilde{\mathbb{D}}\mathbf{d} = \mathbf{0}]_k, \ \ &\forall k : \tilde{V}_k \subset \Omega_N, && \text{(22c)} \end{aligned}$$

where $\boldsymbol{\psi} := \{\psi_k\}_{k=1}^{N_P^N}$ denotes unknowns assigned to each primal vertex in Ω_N. The matrix $\mathbb{X}_\psi \in \mathbb{R}^{N_P \times N_P^N}$ extends $\boldsymbol{\psi}$ by zero to all the primal vertices. This way the zero Dirichlet boundary condition is incorporated. We need the diagonal matrix $(\mathbb{H})_{k,k} = |\tilde{A}_k|/|L_k|$ to transform primal edge integrals to dual face fluxes since the discrete Ampère's law (22b) is defined on dual faces on Ω_N.

Vector of unknowns	Meaning	Vector size
$\mathbf{e}$	line integrals of $\mathbf{E}$-field at primal edges L	N_L
$\boldsymbol{\varphi}$	boundary scalar potential φ at primal vertices P on $\partial\Omega$	N_P^∂
$\mathbf{b}$	surface integrals of $\mathbf{B}$-field at primal faces A	N_A
$\mathbf{h}$	line integrals of $\mathbf{H}$-field at dual edges $\tilde{L}$	$N_{\tilde{L}}$
$\mathbf{d}$	surface integrals of $\mathbf{D}$-field at dual faces $\tilde{A}$	$N_{\tilde{A}}$
$\boldsymbol{\psi}$	Lagrange multiplier ψ at primal vertices P in Ω_N	N_P^N

Tab. 3. Definitions and sizes of the vectors of unknowns.

3.2.4 Numbers of Equations and Unknowns

We can probe the well-posedness of the (semi-)discrete Maxwell system by checking whether the numbers of unknowns (also called degrees of freedom (D.o.F.)) and equations coincide. First, we count mesh entities according to their locations:

$$\begin{aligned}
&\#\text{ primal cells } \quad N_V, && \#\text{ dual cells } \quad N_{\tilde{V}} := N_P,\\
&\#\text{ primal edges } \quad N_L := \underbrace{N_L^C + N_L^I}_{=N_L^\partial} + N_L^\circ, && \#\text{ dual edges } \quad N_{\tilde{L}} := \underbrace{N_{\tilde{L}}^\partial}_{=N_L^\partial} + \underbrace{N_{\tilde{L}}^\circ}_{=N_A},\\
&\#\text{ primal faces } \quad N_A := \underbrace{N_A^C + N_A^I}_{=N_A^\partial} + N_A^\circ, && \#\text{ dual faces } \quad N_{\tilde{A}} := \underbrace{N_{\tilde{A}}^\partial}_{=N_P^\partial} + \underbrace{N_{\tilde{A}}^\circ}_{=N_L},\\
&\#\text{ primal vertices } \quad N_P := \underbrace{N_P^C + N_P^I}_{=N_P^\partial} + N_P^\circ,
\end{aligned}$$

where the superscripts indicate where the entities are located. The equalities $N_{\tilde{L}}^\partial = N_L^\partial, N_{\tilde{A}}^\partial = N_P^\partial$ reveal the bijective relation between the boundary primal entities and auxiliary entities, as can be checked easily by inspecting Fig. 6. We also give a summary of the unknowns in Tab. 3.

Next, we collect all the algebraic equations derived from the Maxwell system and the boundary conditions:

$$\begin{aligned}
\text{discrete Faraday's law (20a)} &\longrightarrow N_A \text{ equations}\\
\text{discrete Ampere's law (20b)} &\longrightarrow N_{\tilde{A}} \text{ equations}\\
\text{discrete material laws (20e)(20f)} &\longrightarrow N_A + N_L \text{ equations}\\
\text{boundary condition (21c)} &\longrightarrow N_P^C \text{ equations}\\
\text{boundary condition (21b)} &\longrightarrow N_L^\partial \text{ equations}\\
\text{boundary condition (21a)} &\longrightarrow N_{\tilde{A}}^I \text{ equations.}\\
\text{vanishing divergence constraint (22c)} &\longrightarrow N_{\tilde{V}}^N \text{ equations.}
\end{aligned}$$

Comparing the numbers of d.o.f. in Tab. 3 and of the equations we collect above, we see that they are equal:

$$\begin{aligned}
\#\text{ of unknowns} &= N_L + N_A + N_{\tilde{L}} + N_{\tilde{A}} + N_P^\partial + N_P^N,\\
\#\text{ of equations} &= N_A + N_{\tilde{A}} + N_A + N_L^\partial + N_L + N_P^C + N_P^I + N_{\tilde{V}}^N.
\end{aligned}$$

Of course, the matching numbers of unknowns and equations do not necessarily result in a valid linear system, since the equations might be linearly dependent. In fact, the linear system will be singular without the stabilization proposed in the previous section when $\lambda = 0$.

3.3 Discrete Euler Equations

We employ the finite volume method (FVM) to discretize the Euler system. The Euler equations (4) can be cast into the form of a conservation law with source terms:

$$\partial_t \mathbf{U} + \nabla \cdot \mathbf{f}(\mathbf{U}) = \mathbf{RHS}, \tag{23}$$

where $\mathbf{U}:\Omega\times[0,T]\to\mathbb{R}^m$ stands for m conservative variables; $\mathbf{f}(\mathbf{U}):\Omega\times[0,T]\to\mathbb{R}^{3\times m}$ is the flux function depending on $\mathbf{U}$; $\mathbf{RHS}:\Omega\times[0,T]\to\mathbb{R}^m$ is the source term. In the case of the full 3D Euler equations (9e), $m=5$ and $\mathbf{U}:=[n,n\mathbf{u},ne]$.

To obtain the semi-discretization, we first integrate (23) over a *dual* cell $\tilde{V}_k\in\Omega_P$

$$\dot{\overline{\mathbf{U}}}_k+\frac{1}{|\tilde{V}_k|}\sum_{l:\tilde{A}_l\in\partial\tilde{V}_k}|\tilde{A}_l|\underbrace{\frac{1}{|\tilde{A}_l|}\iint_{\tilde{A}_l}\mathbf{f}(\mathbf{U})\cdot\mathbf{n}_l\mathrm{d}A}_{:=\overline{\mathbf{f}}_l\approx\mathbf{f}_l^{\mathrm{num}}}=\underbrace{\frac{1}{|\tilde{V}_k|}\iiint_{\tilde{V}_k}\mathbf{RHS}\mathrm{d}V}_{:=\overline{\mathbf{RHS}}_k},\quad k=1,2,\dots,N_{\tilde{V}}^P \tag{24}$$

where $\overline{\mathbf{U}}_k:=\iiint_{\tilde{V}_k}\mathbf{U}\mathrm{d}V/|\tilde{V}_k|\in L^2([0,T],\mathbb{R}^m)$ is the cell average of $\mathbf{U}$ and $\mathbf{n}_l$ is the outer normal vector of face $\tilde{A}_l$ with respect to the cell $\tilde{V}_k$. In FVM, the flux $\overline{\mathbf{f}}_l$ in (24) is approximated by a numerical flux $\mathbf{f}_l^{\mathrm{num}}:=\mathbf{f}^{\mathrm{num}}\left(\overline{\mathbf{U}}_k,\overline{\mathbf{U}}_{\hat{k}(k,l)},\mathbf{n}_l\right)$, where $\hat{k}(k,l)$ returns the index of the adjacent dual cell that shares $\tilde{A}_l$ with cell $\tilde{V}_k$. Classical numerical fluxes include the Lax-Friedrich flux, the Rusanov flux, and the Engquist-Osher flux, see [31, Sec. 12.6]. We end up with the semi-discretized equation:

$$\dot{\overline{\mathbf{U}}}_k+\frac{1}{|V_k|}\sum_{l:\tilde{A}_l\in\partial\tilde{V}_k}|\tilde{A}_l|\mathbf{f}^{\mathrm{num}}\left(\overline{\mathbf{U}}_k,\overline{\mathbf{U}}_{\hat{k}(k,l)},\mathbf{n}_l\right)=\overline{\mathbf{RHS}}_k,\quad k=1,2,\dots,N_{\tilde{V}}^P. \tag{25}$$

We employ the Rusanov flux, which writes

$$\mathbf{f}^{\mathrm{num}}\left(\overline{\mathbf{U}}_L,\overline{\mathbf{U}}_R,\mathbf{n}\right)=\frac{1}{2}\left[\mathbf{f}(\overline{\mathbf{U}}_L)\cdot\mathbf{n}+\mathbf{f}(\overline{\mathbf{U}}_R)\cdot\mathbf{n}\right]-\frac{1}{2}\overline{s}\left(\overline{\mathbf{U}}_R-\overline{\mathbf{U}}_L\right), \tag{26}$$

where $\overline{s}=\max\{s(\overline{\mathbf{U}}_L),s(\overline{\mathbf{U}}_R)\}$ with $s(\mathbf{U}):=|\mathbf{u}\cdot\mathbf{n}|+\sqrt{\gamma p/\rho}$ representing the largest wave speed.

At this stage, we would like to discuss why *the Euler system should be discretized on* $\tilde{\mathcal{M}}$. As is shown in the integrated Ampère's law (17b), the electric currents are defined on dual faces $\tilde{A}$. By solving the Euler equations on $\tilde{\mathcal{M}}$, we have the mass flux on dual faces $\tilde{A}$ as well. In this way, the connection between the charge conservation (3) and the mass conservation (the 1st equation in (4)) due to the current-momentum coupling (5) is preserved on the discrete level.

For the sake of presentation, we rewrite (25) into a matrix form. By abuse of notation, we stack all the cell average $\{\overline{\mathbf{U}}_k\}_{k=1}^{N_{\tilde{V}}^P}$ into a matrix $\mathbf{U}\in\mathbb{R}^{N_{\tilde{V}}^P\times 5}$ with $\mathbf{U}_{k,:}=\overline{\mathbf{U}}_k$. Further, we denote by $\mathbf{F}\in\mathbb{R}^{N_{\tilde{A}}^P\times 5}$ the collection of the (total) numerical fluxes, i.e. $\mathbf{F}_{k,:}=\mathbf{f}_k^{\mathrm{num}}=[f_k^{\mathrm{mass}},\boldsymbol{f}_k^{\mathrm{mom}},f_k^{\mathrm{ene}}]$. In the same way, we denote by $\mathbf{RHS}\in\mathbb{R}^{N_{\tilde{V}}^P\times 5}$ the collection of $\overline{\mathbf{RHS}}_k$. Besides, we define the diagonal matrices $\tilde{\mathbb{V}}\in\mathbb{R}^{N_{\tilde{V}}^P\times N_{\tilde{V}}^P}$ and $\tilde{\mathbb{A}}\in\mathbb{R}^{N_{\tilde{A}}^P\times N_{\tilde{A}}^P}$ with $(\tilde{\mathbb{A}})_{k,k}=|\tilde{A}_k|$. Making use of the incidence matrices, we end up with

$$\dot{\mathbf{U}}+\tilde{\mathbb{V}}^{-1}\tilde{\mathbb{D}}\tilde{\mathbb{A}}\mathbf{F}(\mathbf{U})=\mathbf{RHS}(\mathbf{U},\mathbf{d},\mathbf{b}), \tag{27}$$

Recall that $\tilde{\mathbb{D}}$ represents the discrete divergence of $\tilde{\mathcal{M}}$. Dependence of $\mathbf{RHS}$ on $\mathbf{d},\mathbf{b}$ is implied by (9e) and will be elaborated next.

3.3.1 Reconstruction of Lorentz Force

Since the electromagnetic fields are represented by integrals on edges and faces, we need to reconstruct their vector components for the computation of the Lorentz force (and Joule heating) inside each dual cell. The task involves two aspects:

- given the fluxes at the faces of a cell, reconstruct the vector field inside the cell;
- given the integrals along the edges of a cell, reconstruct the vector field inside the cell.

We adopt the principle of least squares fitting and reconstruct a *constant* vector field inside each cell. For a cell $\tilde{V}$ with N_A faces with areas $\{A_k\}_{k=1}^{N_A}$, normal vectors $\{\mathbf{n}_k\}_{k=1}^{N_A}$ and fluxes $\{f_k\}_{k=1}^{N_A}$, a constant vector field $\mathbf{v}$ satisfying

$$\mathbf{v}=\arg\min_{\mathbf{w}\in\mathbb{R}^3}\sum_{k=1}^{N_A}(A_k\mathbf{w}\cdot\mathbf{n}_k-f_k)^2$$

can be computed through

$$\mathbf{v} = (\mathbb{K}^T\mathbb{K})^{-1}\mathbb{K}^T\mathbf{f},$$

where

$$\mathbb{K} = [A_1\mathbf{n}_1, A_2\mathbf{n}_2, \dots, A_{N_A}\mathbf{n}_{N_A}]^T, \quad \mathbf{f} = [f_1, f_2, \dots, f_{N_A}]^T,$$

and each vector in $\mathbb{R}^3$ is treated as a column vector. The construction based on the integral quantities on edges can be done similarly. Assembling the local constructions for each dual cell, the global construction can be written as

$$\mathbf{E} = \tilde{\mathbb{R}}_E\mathbf{d}\ , \quad \mathbf{B} = \tilde{\mathbb{R}}_B\mathbf{b}, \tag{28}$$

where $\mathbf{d}, \mathbf{b}$ are defined in Tab. 3; $\mathbf{E} := \{\mathbf{E}_k\}_{k=1}^{N_{\tilde{V}}}$ and $\mathbf{B} := \{\mathbf{B}_k\}_{k=1}^{N_{\tilde{V}}}$ are $N_{\tilde{V}} \times 3$ matrices containing the reconstructed **E**-fields and **B**-fields at each $\tilde{V}$; $\tilde{\mathbb{R}}_E$ and $\tilde{\mathbb{R}}_B$ are thus rank-3 tensors.

The problem of the reconstruction of vector fields on unstructured meshes is a widely studied topic. Apart from the least-squares method, other methods include Perot's method [41], finite-entity-based methods, etc., which potentially can achieve higher-order accuracy. See [15, Sec. 3.4.4] and the references therein.

Eventually, the right-hand-side term in (27) can be computed by evaluating the right-hand-side of rescaled Euler equations (9e) for the reconstructed **E**-field and **B**-field by (28) defined in each dual cell.

3.3.2 Discrete Boundary Conditions

The boundary conditions for the Euler system (see Sec. 2.4) are implemented by the approach of ghost cells [32, Chapt. 7], i.e. extending the domain by a layer of virtual cells with prescribed variables. In our case, the ghost cells at the open boundary at Γ_C are assigned the same state as their adjacent interior cells. It is equivalent to enforcing the numerical fluxes

$$\mathbf{F}_k = \mathbf{f}^{\text{num}}(\mathbf{U}_l, \mathbf{U}_l, \mathbf{n}_k), \quad \forall k : \tilde{A}_k \subset \Gamma_C, \tag{29}$$

where l refers to the (unique!) index of the cell adjacent to the boundary face $\tilde{A}_k$. For the *reflective wall* Γ_W, the momentum of a ghost cell is reversed with respect to its adjacent interior cell while keeping the other quantities unchanged. Therefore, in this case the numerical fluxes are

$$\mathbf{F}_k = \mathbf{f}^{\text{num}}(\mathbf{U}_l, \hat{\mathbf{U}}_l, \mathbf{n}_k), \quad \forall k : \tilde{A}_k \subset \Gamma_W, \tag{30}$$

where the state of the ghost cell $\hat{\mathbf{U}}_l = [n, n\mathbf{u} - 2(\mathbf{n}\cdot\mathbf{u})\mathbf{n}, ne]^T$ reverses the normal velocity of $\mathbf{U}_l = [n, n\mathbf{u}, ne]^T$.

3.4 Summary: Spatially Semi-discrete Model

We collect all the equations and boundary conditions presented above and give a summary for the spatially semi-discrete Maxwell-Euler system based on the FIT/DEC-FVM framework:

$$(20a) \implies [\dot{\mathbf{b}} + \mathbb{C}\mathbf{e} = \mathbf{0}]_k, \quad \forall k : A_k \subset \Omega, \tag{31a}$$

$$(20b) \implies [\dot{\mathbf{d}} - \tilde{\mathbb{C}}\mathbf{h} = -\Sigma_* q_* \boldsymbol{f}_*^{\text{mass}}]_k, \quad \forall k : \tilde{A}_k \subset \Omega_P, \tag{31b}$$

$$(22b) \implies [\dot{\mathbf{d}} - \tilde{\mathbb{C}}\mathbf{h} + \mathbb{H}\mathbb{G}\mathbb{X}_\psi\boldsymbol{\psi} = \mathbf{0}]_k, \quad \forall k : \tilde{A}_k \subset \Omega_N, \tag{31c}$$

$$(22c) \implies [\tilde{\mathbb{D}}\mathbf{d} = \mathbf{0}]_k, \quad \forall k : \tilde{V}_k \subset \Omega_N, \tag{31d}$$

$$(27) \implies [\dot{\mathbf{U}}_* + \tilde{\mathbb{V}}^{-1}\tilde{\mathbb{D}}\tilde{\mathbb{A}}\mathbf{F}_* = \mathbf{RHS}_*]_k, \quad \forall k : \tilde{V}_i \subset \Omega_P, \tag{31e}$$

$$(20e) \implies [\mathbf{h} = \mathbb{M}_\mu^{-1}\mathbf{b}]_k, \quad \forall k : A_k \subset \Omega, \tag{31f}$$

$$(20f) \implies [\mathbf{d} = \mathbb{M}_\epsilon\mathbf{e}]_k, \quad \forall k : L_k \subset \Omega, \tag{31g}$$

where $* \in \{e, i, \dots\}$ and $\boldsymbol{f}^{\text{mass}}$ denotes the mass flux which is defined in Sec. 3.3. By $[\dots]_k$ we mean taking the k-th component of both sides of the equation. We have the following boundary conditions:

$$(21a) \implies d_k = 0, \quad \forall k : \tilde{A}_k \subset \Gamma_I, \tag{31h}$$

$$(21b) \implies e_k = (\mathbb{G}\mathbb{X}_\varphi\boldsymbol{\varphi})_k, \quad \forall k : L_k \subset \partial\Omega, \tag{31i}$$

$$(21c) \implies \varphi_k = \varphi^{\pm}(t), \quad \forall k : P_k \subset \Gamma_C^{\pm}, \tag{31j}$$

$$(29) \implies \mathbf{F}_{*,k} = \mathbf{f}^{\text{num}}(\mathbf{U}_{*,l}, \mathbf{U}_{*,l}, \mathbf{n}_k), \quad \forall k : \tilde{A}_k \subset \Gamma_C, \tag{31k}$$

$$(30) \implies \mathbf{F}_{*,k} = \mathbf{f}^{\text{num}}(\mathbf{U}_{*,l}, \hat{\mathbf{U}}_{*,l}, \mathbf{n}_k), \quad \forall k : \tilde{A}_k \subset \Gamma_W. \tag{31l}$$

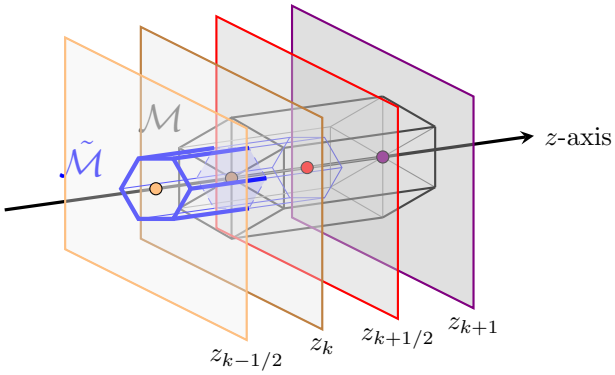

Fig. 7. "Projection" of a 3D discretization to 1D. On the assumption of transverse translation invariance, we can reduce all the degrees of freedom lying in the perpendicular plane $z = z_k$ to the vertex at $z = z_k$. For instance, an edge orthogonal to the z-axis is projected to a vertex on the z-axis while a parallel edge to the z-axis is projected to an edge on the z-axis.

We would like to stress again that in our FIT/DEC-FVM framework Faraday's law is discretized on the primal mesh $\mathcal{M}$ while Ampère's law is discretized on the dual mesh $\tilde{\mathcal{M}}$. The material laws directly connect primal and dual d.o.f. Using the cells of the dual mesh $\tilde{\mathcal{M}}$ as finite-volumes for the Euler system the connection between electric currents and fluid momenta is perfectly represented in the discretization, since both are defined on the dual faces.

4 Full Discretization

4.1 Motivation: Reduction to One Spatial Dimension

Our work extends the 1D scheme proposed in [11] to three dimensions. Therefore, it is supposed to be compatible with the original 1D scheme when "projected" to one dimension. This perspective helps to understand how the 3D scheme is linked to the 1D. For the sake of presentation, we discuss the one-fluid model of [11], for which ions are assumed immobile and only the motion of electrons is considered.

4.1.1 Projection to One Dimension

Consider a primal-dual mesh pair $(\mathcal{M}, \tilde{\mathcal{M}})$ that is constructed by 2D extrusion along the z-axis and is unbounded in transverse directions. Assuming transverse translation invariance and rotational symmetry, we can "project" all the d.o.f. onto the z-axis. The idea is sketched in Fig. 7.

In [11], the authors investigate a 1D Maxwell-Euler system by assuming vanishing traverse derivatives. For further simplicity, a transverse mode is considered, i.e. u_y, E_y, B_x, and B_z are set to zero. The 1D reduced component-wise one-fluid Maxwell-Euler system and its quasi-neutral limit are

$$
\begin{aligned}
(9e) \implies & \begin{cases} \partial_t n + \partial_z(n u_z) = 0, \\ \varepsilon^2[\partial_t(n u_x) + \partial_z(n u_z u_x)] = -n(E_x - u_z B_y), \\ \varepsilon^2[\partial_t(n u_z) + \partial_z(n u_z^2)] + \partial_z(p(n)) = -n(E_z + u_x B_y), \end{cases} \\
(9a) \implies & \partial_t B_y + \partial_z E_x = 0, \\
(9b) \implies & \begin{cases} \lambda^2 \partial_t E_x + \partial_z B_y = n u_x, \\ \lambda^2 \partial_t E_z = n u_z, \end{cases} \\
(9d) \implies & \lambda^2 \partial_z E_z = 1 - n,
\end{aligned}
\quad \xrightarrow{\lambda \to 0} \quad
\begin{aligned}
n &= 1, \\
\varepsilon^2 \partial_t(u_x) &= -E_x, \\
E_z + u_x B_y &= 0, \\
u_z &= 0, \\
\partial_t B_y + \partial_z E_x &= 0, \\
\partial_z B_y &= n u_x,
\end{aligned}
$$

where all the fluid variables are attributed to electrons and the subscript indicates the direction of the component. An isentropic fluid model with the equation of state $p(n) = n^\gamma$ is assumed to drop the energy equation.

4.1.2 1D Fully Discrete Plasma Model

The fully discrete scheme proposed in [11] is given below. From now on, the superscript m for any variable indicates the time step. The scheme is built on a uniform 1D mesh with cell size h and evolves the system with time step size $\delta^m := t^{m+1} - t^m$:

$$
(31e) \implies \begin{cases}
\dfrac{n_k^{m+1} - n_k^m}{\delta^m} + \dfrac{f^{\mathrm{mass},m+1/2}_{k+1/2} - f^{\mathrm{mass},m+1/2}_{k-1/2}}{h} = 0, \\
\dfrac{(nu_x)_k^{m+1} - (nu_x)_k^m}{\delta^m} + \dfrac{f^{\mathrm{mom}_x,m}_{k+1/2} - f^{\mathrm{mom}_x,m}_{k-1/2}}{h} = -\dfrac{n_k^m E^{m+1}_{x,k}}{\varepsilon^2} + \dfrac{n_k^m u^m_{z,k} \tilde{B}^m_{y,k}}{\varepsilon^2}, \\
\dfrac{(nu_z)_k^{m+1} - (nu_z)_k^m}{\delta^m} + \dfrac{f^{\mathrm{mom}_z,m}_{k+1/2} - f^{\mathrm{mom}_z,m}_{k-1/2}}{h} = -\dfrac{n_k^m \tilde{E}^{m+1}_{z,k}}{\varepsilon^2} - \dfrac{n_k^m u^m_{x,k} \tilde{B}^m_{y,k}}{\varepsilon^2},
\end{cases}
$$

$$
(31a) \implies \quad \frac{B^{m+1}_{y,k+1/2} - B^m_{y,k+1/2}}{\delta^m} + \frac{E^{m+1}_{x,k+1} - E^{m+1}_{x,k}}{h} = 0,
$$

$$
(31b) \implies \begin{cases}
\lambda^2 \dfrac{E^{m+1}_{x,k} - E^m_{x,k}}{\delta^m} + \dfrac{B^{m+1}_{y,k+1/2} - B^{m+1}_{y,k-1/2}}{h} = (nu_x)^{m+1}_k, \\
\lambda^2 \dfrac{E^{m+1}_{z,k+1/2} - E^m_{z,k+1/2}}{\delta^m} = f^{\mathrm{mass},m+1/2}_{k+1/2},
\end{cases}
$$

where

$$
(28) \implies \quad \tilde{E}^m_{z,k} = \frac{1}{2}(E^m_{z,k+1/2} + E^m_{z,k-1/2}), \quad \tilde{B}^m_{y,k} = \frac{1}{2}(B^m_{y,k+1/2} + B^m_{y,k-1/2}),
$$

are the averaged electromagnetic fields, and the fluxes read

$$
(26) \implies \begin{cases}
f^{\mathrm{mass},m+1/2}_{k+1/2} = \dfrac{1}{2}[(nu_z)^{m+1}_k + (nu_z)^{m+1}_{k+1} + \mu^m_{k+1/2}(n^m_k - n^m_{k+1})], \\
f^{\mathrm{mom}_x,m}_{k+1/2} = \dfrac{1}{2}[(nu_z u_x)^m_k + (nu_z u_x)^m_{k+1} + \mu^m_{k+1/2}((nu_x)^m_k - (nu_x)^m_{k+1})], \\
f^{\mathrm{mom}_z,m}_{k+1/2} = \dfrac{1}{2}[(nu_z^2 + p(n)/\varepsilon^2)^m_k + (nu_z^2 + p(n)/\varepsilon^2)^m_{k+1} + \mu^m_{k+1/2}((nu_z)^m_k - (nu_z)^m_{k+1})].
\end{cases}
$$

The implicit terms are highlighted and are all essential to achieve the AP property. The implicitness of the electric field in the Lorentz force is shown to be necessary in [12] for the Euler-Poisson system. In [11], based on the linearized stability analysis, the author shows that the full-implicit treatment of the Maxwell equations is essential to achieve stability in the quasi-neutral limit. Besides, the mass flux in the mass conservation equation and the current in Ampère's law has the same level of implicitness to guarantee consistency with Gauss's law.

4.2 Semi-implicit Fully-discrete AP Scheme in 3D

Taking the cue from the formulas of Sec. 4.1.2 and combining the 3D FIT/DEC-FVM framework presented in Sec. 3 and the time-stepping scheme shown below, we propose the following semi-implicit fully-discrete AP

scheme in 3D:

$$(31a) \implies \left[\delta_m^{-1}(\mathbf{b}^{m+1}-\mathbf{b}^m)+\mathbb{C}\,\mathbf{e}^{m+1}=\mathbf{0}\right]_k, \quad \forall k: A_k\subset\Omega, \tag{32a}$$

$$(31b) \implies \left[\lambda^2\delta_m^{-1}(\mathbf{d}^{m+1}-\mathbf{d}^m)-\tilde{\mathbb{C}}\,\mathbf{h}^{m+1}=-\Sigma_* q_*\,\boldsymbol{f}_*^{\mathrm{mass},m+1/2}\right]_k, \quad \forall k: \tilde{A}_k\subset\Omega_P, \tag{32b}$$

$$(31c) \implies \left[\lambda^2\delta_m^{-1}(\mathbf{d}^{m+1}-\mathbf{d}^m)-\tilde{\mathbb{C}}\,\mathbf{h}^{m+1}+\mathbb{H}\mathbb{G}\mathbb{X}_\psi\,\boldsymbol{\psi}^{m+1}=\mathbf{0}\right]_k, \quad \forall k: \tilde{A}_k\subset\Omega_N, \tag{32c}$$

$$(31d) \implies \left[\tilde{\mathbb{D}}\,\mathbf{d}^{m+1}=\mathbf{0}\right]_k, \quad \forall k: \tilde{V}_k\subset\Omega_N, \tag{32d}$$

$$(31e) \implies \left[\delta_m^{-1}(\mathbf{U}_*^{m+1}-\mathbf{U}_*^m)+\tilde{\mathbb{V}}^{-1}\tilde{\mathbb{D}}\tilde{\mathbb{A}}\,\mathbf{F}_*^{m+1/2}=\mathbf{RHS}_*^{m+1/2}\right]_k, \quad \forall k: \tilde{V}_k\subset\Omega_P, \tag{32e}$$

$$(31f) \implies [\mathbf{h}^{m+1}=\mathbb{M}_\mu^{-1}\mathbf{b}^{m+1}]_k, \quad \forall k: A_k\subset\Omega, \tag{32f}$$

$$(31g) \implies [\mathbf{d}^{m+1}=\mathbb{M}_\epsilon\mathbf{e}^{m+1}]_k, \quad \forall k: L_k\subset\Omega, \tag{32g}$$

where

$$\mathbf{U}_{*,k}^m=\begin{pmatrix} n\\ n\mathbf{u}\\ ne\end{pmatrix}_{*,k}^m, \tag{32h}$$

$$\mathbf{F}_{*,k}^{m+1/2}=\begin{pmatrix} f^{\mathrm{mass},m+1/2}\\ \boldsymbol{f}^{\mathrm{mom},m}\\ f^{\mathrm{ene},m}\end{pmatrix}_{*,k}=\begin{pmatrix} \frac{1}{2}\left[(nu_\perp)_L^{m+1}+(nu_\perp)_R^{m+1}\right]-\frac{1}{2}s^m(n_R^m-n_L^m)\\ \frac{1}{2}\left[(nu_\perp\mathbf{u})_L^m+(nu_\perp\mathbf{u})_R^m+p_L^m\mathbf{n}_j+p_R^m\mathbf{n}_j\right]-\frac{1}{2}s^m\left[(n\mathbf{u})_R^m-(n\mathbf{u})_L^m\right]\\ \frac{1}{2}\left[(nhu_\perp)_L^m+(nhu_\perp)_R^m\right]-\frac{1}{2}s^m\left[(ne)_R^m-(ne)_L^m\right]\end{pmatrix}_{*,k}, \tag{32i}$$

$$\mathbf{RHS}_{*,k}^{m+1/2}=\begin{pmatrix} 0\\ \varepsilon_*^{-2}q_*\left[n_*^m\,\mathbf{E}^{m+1}+(n\mathbf{u})_*^m\times\mathbf{B}^m\right]\\ \varepsilon_*^{-2}q_*(n\mathbf{u})_*^m\cdot\mathbf{E}^{m+1}\end{pmatrix}_k+\begin{pmatrix} 0\\ \varepsilon_*^{-2}\,\mathbf{R}_*^{\mathrm{coll},m+1}\\ \varepsilon_*^{-2}\,Q_*^{\mathrm{coll},m+1}\end{pmatrix}_k, \tag{32j}$$

$$\mathbf{E}^{m+1}=\tilde{\mathbb{R}}_E\mathbf{d}^{m+1}, \quad \mathbf{B}^m=\tilde{\mathbb{R}}_B\mathbf{b}^m, \tag{32k}$$

$$\mathbf{R}_{*,k}^{\mathrm{coll},m+1}=\begin{cases}\alpha^{\mathrm{coll}}\left[n_e^m\,(n\mathbf{u})_i^{m+1}-n_i^m\,(n\mathbf{u})_e^{m+1}\right]_k, & \text{if } *=e\\ \alpha^{\mathrm{coll}}\left[n_i^m\,(n\mathbf{u})_e^{m+1}-n_e^m\,(n\mathbf{u})_i^{m+1}\right]_k, & \text{if } *=i\end{cases} \tag{32l}$$

$$Q_{*,k}^{\mathrm{coll},m+1}=\mathbf{R}_{*,k}^{\mathrm{coll},m+1}\cdot\mathbf{u}_{*,k}^{m+1}. \tag{32m}$$

A superscript $m+1/2$ indicate a dependence on the quantities at both time step m and $(m+1)$. In the Rusanov flux (32i), we denote by $u_\perp$ the normal component of the velocity $\mathbf{u}$ with respect to the dual face $\tilde{A}_k$. For the sake of simplicity we have confine the presentation of the collision term (32l) (32m) to the two-species case.

The time-stepping scheme mimics the 1D scheme shown in the previous section. The implicit treatment of the friction term is necessary owing to its potential stiffness in case the prefactor $\varepsilon_*^{-2}\alpha^{\mathrm{coll}}$ attains a large value.

Remark. *When applying the "projection to one dimension" described in Sec. 4.1.1, the fully discrete 3D AP scheme (32a)-(32m) collapses to the scheme of [11] presented in Sec. 4.1.2. This is not a coincidence, because recovering that scheme under dimensional reduction has guided our construction.*

Remark. *The AP scheme aims to remove the λ-dependence of the stability constraint on the time step size. Yet time-step size for the fully discrete Euler system is still limited by a CFL condition due to the explicit treatment of the fluid convection.*

4.2.1 Linearly Implicit Time-stepping

The semi-implicit scheme (32a)-(32m) merely entails solving a linear system in each time step. A single time step comprises the following computations:

Step 1. We establish the connection between $\mathbf{f}_*^{\mathrm{mass},m+1/2}$ and $\mathbf{d}$ through the momentum equation (see (32e)(32i)(32j)). Relying on the reconstruction (28), the following formula emerges:

$$(n\mathbf{u})_*^{m+1} = \hat{\mathbb{M}}_*^m \mathbf{d}^{m+1} + \boldsymbol{\eta}_*^m. \tag{33}$$

The expression for the current $\mathbf{J}^{m+1}$ in Ω_P (see (32b)) depends on the mass flux $\boldsymbol{f}_*^{\mathrm{mass},m+1}$ which, in turn, relies on $(n\mathbf{u})_*^{m+1}$ through (32i). Appealing to (33), one can formulate the following relation:

$$\mathbf{j}^{m+1} := \Sigma_* q_* \boldsymbol{f}_*^{\mathrm{mass},m+1} = \mathbb{M}_\sigma^m \mathbf{d}^{m+1} + \mathbf{j}_{\mathrm{aux}}^m, \tag{34}$$

where $\mathbb{M}_\sigma^m \in \mathbb{R}^{N_{\bar{A}} \times N_{\bar{A}}}$ and $\mathbf{j}_{\mathrm{aux}}^m \in \mathbb{R}^{N_{\bar{A}}}$. The formulas of $\hat{\mathbb{M}}_*^m, \boldsymbol{\eta}_*^m, \mathbb{M}_\sigma^m, \mathbf{j}_{\mathrm{aux}}^m$ are slightly lengthy but straightforward, so we omit the details.
Step 2. After (34) has been evaluated, the discrete Maxwell system (32a)-(32d) is closed and can be evolved by solving a linear system.
Step 3. With $\mathbf{d}^{m+1}$ at our disposal, we update the momenta $(n\mathbf{u})_*^{m+1}$ according to (33).
Step 4. The remainder of the Euler system can be evolved explicitly.

Remark. *The formula (34) functions as Ohm's law on the discrete level. Matrix $\mathbb{M}_\sigma^m$ can be treated as a "conductivity" matrix. In the quasi-neutral limit $\lambda \to 0$ we lose control of the* $\mathbf{E}$*-field through its time derivative. Therefore, $\mathbb{M}_\sigma^m$ is crucial to the stability of the scheme. Since* $\mathbf{j}$ *and* $\mathbf{d}$ *are both defined on dual faces, it is reasonable to adopt a local relation between them. Therefore, we perform the* diagonal lumping *trick, i.e. rendering $\mathbb{M}_\sigma^m$ diagonal by accumulating the row sum. The lumped $\mathbb{M}_\sigma^m$ has a positive diagonal (for the entity corresponding to Ω_P. the rest is zero since no current exists in Ω_N). Enhanced stability is observed in the numerical experiments with very minor changes in the results.*

5 Numerical Tests

We conduct numerical tests based on the geometric setting and boundary conditions as presented in Sec. 2.4. The primal-dual mesh pair $(\mathcal{M}, \tilde{\mathcal{M}})$ is generated as explained in [15, Chapt. 1]. Examples are shown in Fig. 5. We consider a two-fluid plasma model, which comprises electrons and ions. We set the mass ratio $\varepsilon_e := m_e/m_i = 10^4$ and the collision parameter $\alpha^{\mathrm{coll}} = 32$. All source codes plus instructions for use are available from `https://github.com/TianweiCSE/APPM`.

5.1 Case I: Quasi-1D Problem

Exploiting the radial symmetry of the domain as well as of the boundary conditions, we can simplify the governing equations defined at the axis of symmetry, i.e. z-axis in this case, assuming vanishing radial components of the vector fields and their radial derivatives. The (isentropic and collisionless) Euler-Maxwell system at the axis of symmetry reduces to

$$\begin{aligned}
&\partial_t n_* + \partial_z(n_* u_{*,z}) = 0,\\
&\partial_t(n_* u_{*,z}) + \partial_z(n_* u_{*,z}^2) + \varepsilon_*^{-2}\partial_z p_*(n_*) = \varepsilon_*^{-2} q_* n_* E_z,\\
&\lambda^2 \partial_t E_z = \sum_* -q_* n_* u_{*,z}.
\end{aligned}$$

which is nothing but the 1D model in Sec. 4.1.1 after further dropping u_x, B_y, E_x. We compare the results produced by the 1D scheme (see Sec. 4.1.2) and those produced by the 3D scheme (see Sec. 4.2) restricted to the z-axis. The following initial conditions are used for both models

$$n_e(z,0) = n_i(z,0) = 1, u_z(z,0) = \chi_{[-0.1,0]}(z) - \chi_{[0,0.1]}(z) \quad \forall z \in [-0.1, 0.1],$$

where χ is the characteristic function. The other variables are initially zero. Results for the choice $\lambda = 1$ are given in Fig. 8 and demonstrate good matching.

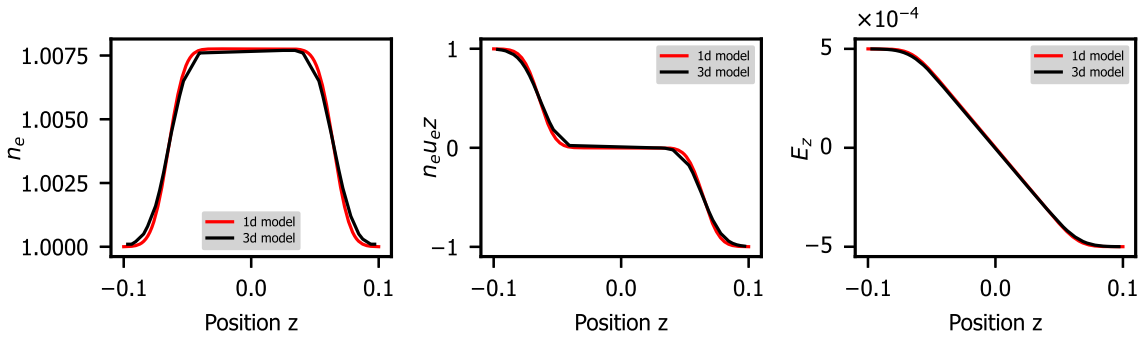

Fig. 8. Case I, $\lambda = 1$: Comparison of 1D two-fluid model and of 3D results (at time $t = 5 \times 10^{-4}$) projected onto the z-axis. The simulations were both conducted on meshes with 64 cells along the z-axis. No friction terms were taken into account. The 3D fields are computed for the axi-symmetric geometry shown in Fig. 2 and then restricted to the z-axis. They slightly differ from 1D results, possibly due to the impact of the cut-off boundary of the 3D domain.

5.2 Case II, convergence: 3D "cuboid domain"

We rely on the geometry from Fig. 1b and the setting in Fig. 2. The computational domain is equipped with structured Cartesian meshes in Fig. 5b. The initial conditions are

$$n_*(\mathbf{x}, 0) = 1, \quad p_*(\mathbf{x}, 0) = 1, \quad \forall \mathbf{x} \in \Omega, * \in \{e, i\},$$

and zero for the other variables. We set $\varphi(\mathbf{x}, t)|_{\Gamma_C^-} = 0, \varphi(\mathbf{x}, t)|_{\Gamma_C^+} = 10 \times t$, that is, one electrode is grounded and a ramp voltage is applied on the other electrode. The results are computed for final time $t = 0.01$. The scheme is tested for different mesh resolutions and the convergence rates are estimated. Tab. 4 lists the errors for the **E**-field, **B**-field, and electron densities with reference solutions generated on a sufficiently fine mesh with $2^{18} = 262144$ primal cells. The results confirm uniform algebraic convergence over $0 \leq \lambda \leq 1$, a vindication of the AP property. It is natural that the convergence rate does not exceed 1, since the reconstruction of the electromagnetic field discussed in Sec. 3.3.1 is only of first order and the numerical flux used for solving the Euler equations is also of first order. The 1/2-order reduction observed for the L^2-error of the **E**-field and the electron density is possibly the consequence of singularities of the solution due to abutting different types of boundary conditions (electrodes and insulating boundary).

5.3 Case III: 3D cylindrical domain

We stick to the setting in Fig. 2 and the mesh in Fig. 5a using the following initial conditions

$$n_*(\mathbf{x}, 0) = 1, \quad p_*(\mathbf{x}, 0) = 1, \quad \forall \mathbf{x} \in \Omega, * \in \{e, i\}.$$

All the other variables are set to zero initially. We set $\varphi(\mathbf{x}, t)|_{\Gamma_C^-} = 0, \varphi(\mathbf{x}, t)|_{\Gamma_C^+} = \tanh(100 \times t)$, that is, a smooth voltage jump is applied at the anode and excites the system.

The cylindrical domain is 5.0 in length and 1.5 in radius. The plasma domain Ω_P is 1.0 in radius, i.e. the non-conducting domain Ω_N has an inner radius of 1.0 and an outer radius of 1.5.

In Fig. 9, the numerical solutions for $\lambda = 1.0, 0.1$ and 0 are shown to visualize the 3D structure of the electromagnetic field. Qualitative verification can be done in many aspects. First, the rotational symmetry of the problem is preserved. Second, the **E**-field points from Γ_C^+ to Γ_C^- with a relatively uniform value of approximately 0.2 (= applied voltage/cylinder length) as a consequence of the irrotational **E**-field in the steady state according to Faraday's law (which is also confirmed in Fig. 11 **(b)**). Note that it does not hold for $\lambda = 1$ since the system has a large characteristic time and takes a long time to reach an equilibrium, as will be shown later in Fig. 10. Besides, the **B**-field is azimuthal (vortex-shaped) and orthogonal to the **E**-field. Also, under the electric force, the electrons move towards the anode Γ_C^+ as expected.

To inspect how the system evolves, the time histories of some quantities are displayed in Fig. 10. Being in stable equilibrium at $t = 0$, the system is excited by applying a voltage and this triggers oscillations that decay over time. A larger value of λ leads to oscillations with larger amplitude and slower damping, whereas

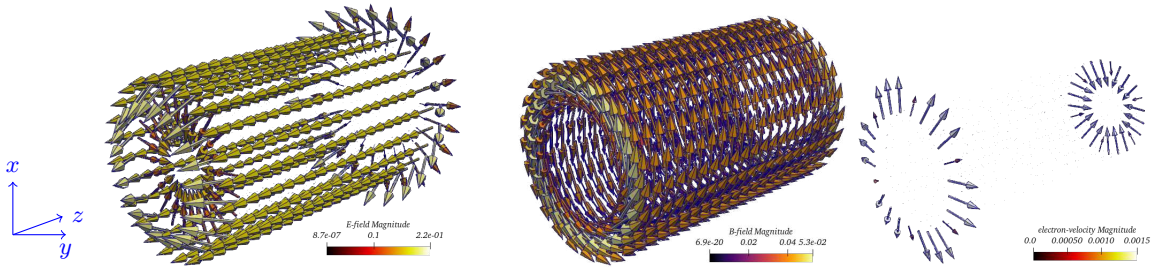

(a) $\lambda = 1.0$

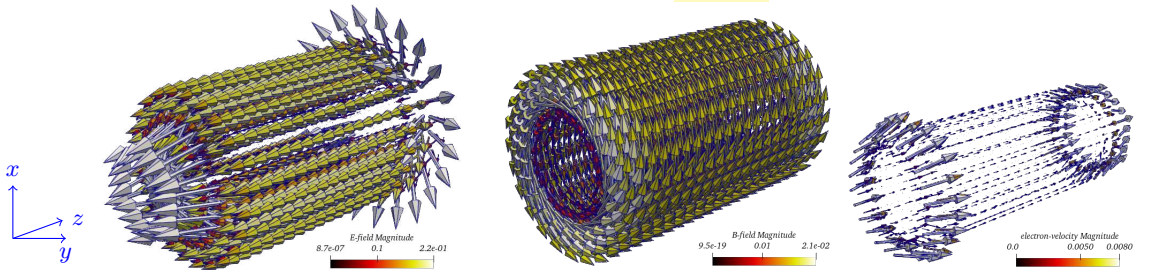

(b) $\lambda = 0.1$

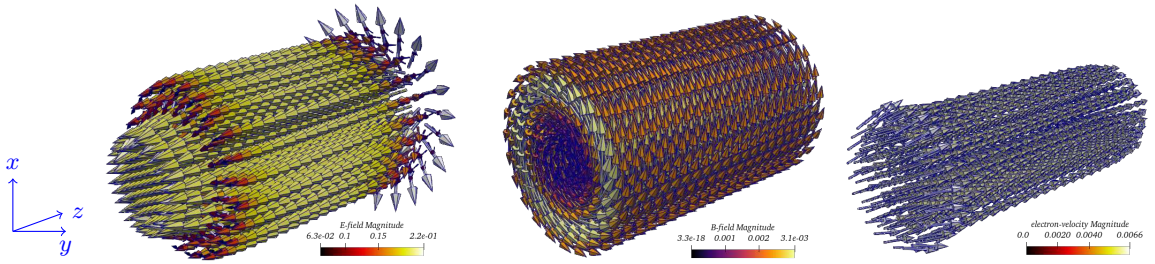

(c) $\lambda = 0.0$

Fig. 9. Case III: Snapshots of the **E**-field, **B**-field, and $\mathbf{u}_e$ for different values of λ at $t = 0.5$.

N_V	**E**-field		**B**-field		electron density	
	L^1-error	L^2-error	L^1-error	L^2-error	L^1-error	L^2-error
64	0.369	0.0712	5.88	1.14	6.67	1.83
512	0.195	0.0493	3.13	0.77	3.09	1.36
4096	0.087	0.0332	0.98	0.34	1.26	0.76
aver. rate	1.05	0.55	1.34	0.90	1.21	0.65

(a) $\lambda = 1$

N_V	**E**-field		**B**-field		electron density	
	L^1-error	L^2-error	L^1-error	L^2-error	L^1-error	L^2-error
64	0.141	0.0271	1.52E-3	2.67E-4	6.67	1.83
512	0.094	0.0214	8.21E-4	1.47E-4	3.09	1.36
4096	0.041	0.0113	3.84E-4	6.93E-5	1.26	0.76
aver. rate	0.93	0.66	1.00	0.98	1.21	0.65

(b) $\lambda = 0.01$

N_V	**E**-field		**B**-field		electron density	
	L^1-error	L^2-error	L^1-error	L^2-error	L^1-error	L^2-error
64	0.127	0.0274	9.46E-4	1.58E-4	6.67	1.83
512	0.100	0.0212	6.26E-4	1.05E-4	3.09	1.36
4096	0.038	0.0110	2.49E-4	4.33E-5	1.26	0.76
aver. rate	0.96	0.69	1.00	0.98	1.21	0.65

(c) $\lambda = 0$

Tab. 4. Case II: L^1 and L^2 errors of the **E**-field, the **B**-field, and the electron density and their convergence rates for different values of λ. The reference solution is computed at a sufficient mesh resolution with $2^{18} = 262144$ primal cells.

for a smaller λ the system quickly reaches a steady state. It is consistent with the fact that λ characterizes the timescale of the electromagnetic field. From a different perspective, it is a reflection of the shielding effect of the plasma which is characterized by the Debye length. Besides, the electrons move much faster and oscillate more than ions as a consequence of the large difference in inertia. Furthermore, the structure-preserving property of our scheme is revealed by the exact balance of the currents at Γ_C^+ and Γ_C^- [22], as is shown in the bottom plot in Fig. 10.

The stabilization proposed in Sec. 3.2.3 is essential to achieve good results when λ tends to zero. As is shown in Fig. 11 **(a)**, the scheme without stabilization incurs a blow-up when λ is close to zero. The proposed stabilization clearly offers a remedy.

The capability of our approach to deal with the non-neutral ($\lambda = \mathcal{O}(1)$) and quasi-neutral ($\lambda = 0$) regimes manifests itself in the reported numerical tests in that valid results are produced for different values of λ including $\lambda = 0$. It is instructive to verify the quasi-neutrality condition (10d) when $\lambda = 0$. To that end we display the **E**-field and particle densities on the z-axis in Fig. 11 **(b)**. The bottom plot demonstrates that the density profiles of the electrons and ions offset each other also for computed quantities: Quasi-neutrality holds on the discrete level.

5.4 Case IV: 3D curved cylindrical domain

To demonstrate the performance of the proposed scheme in more general three-dimensional settings, we bend the cylinder domain in Case III (see Fig. 2), as is shown in Fig. 12. The same initial and boundary conditions as in Case III are imposed. Primal and dual meshes with straight edges and flat faces are generated by extrusion in the direction of a bent central axis.

The numerical approximations of the electromagnetic fields for $\lambda = 0$ and 1 are displayed in Fig. 13. We

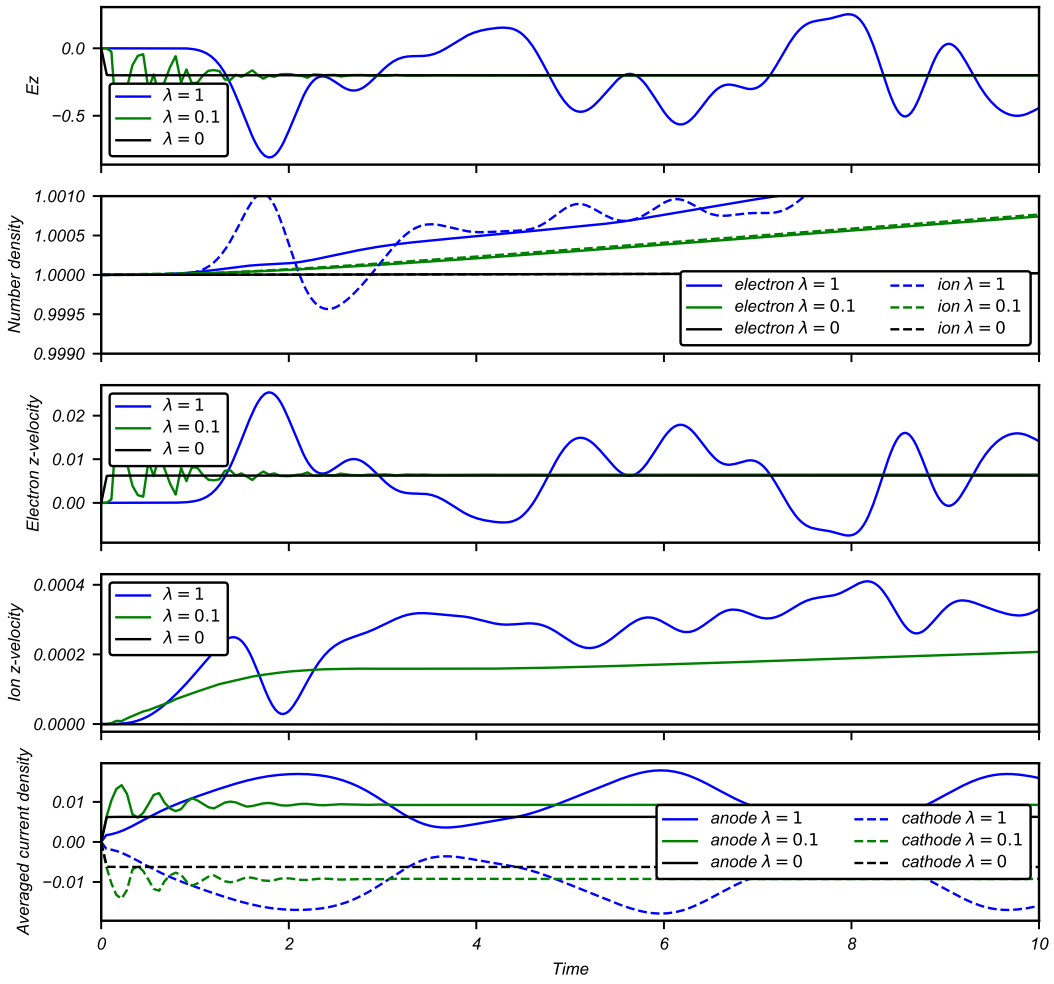

Fig. 10. Case III: Time histories of quantities at the domain center and of the averaged current densities at Γ_C^+ (anode) and Γ_C^- (cathode) for different values of λ. The simulations are done on a mesh with 1920 primal cells with 8 layers along the z-axis.

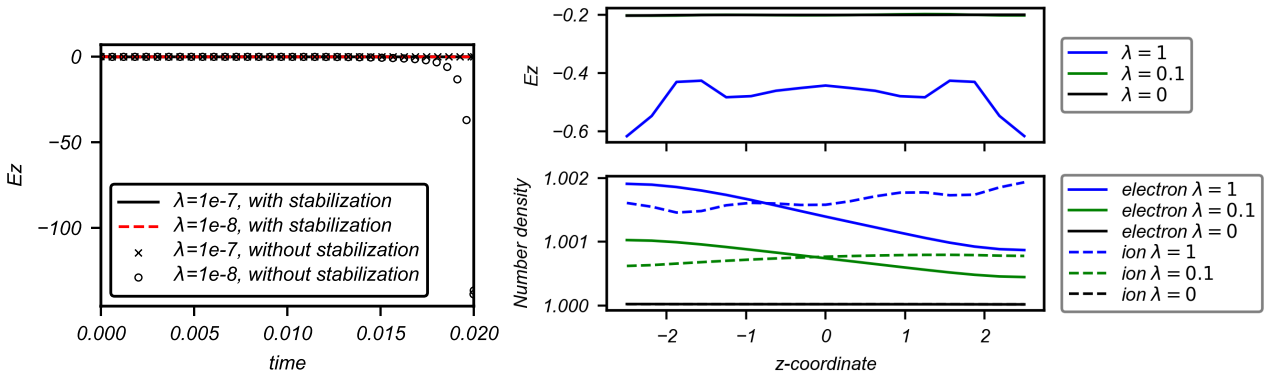

(a) Time-dependent z-component of the **E**-field in a boundary cell on Ω_N

(b) Quantities along z-axis for different λ; the results are computed at $t = 10$ on a mesh with 1920 primal cells and 8 layers along z-axis.

Fig. 11. Case III: **(a)** Stabilization in the non-conducting domain Ω_N, **(b)** Numerical quasi-neutrality.

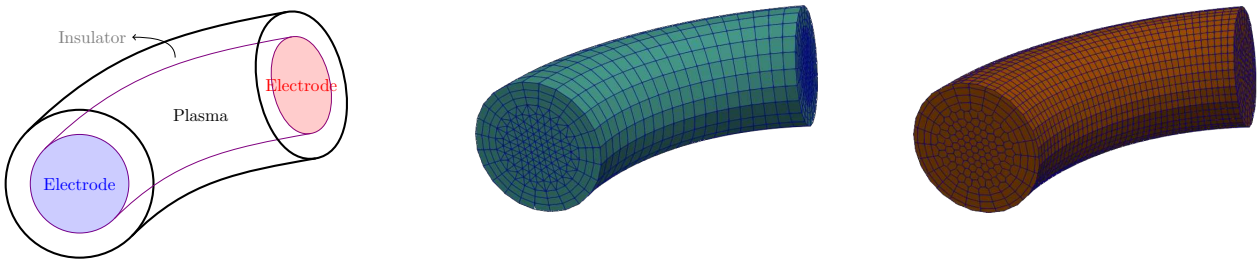

Fig. 12. Case IV: geometry (left); primal mesh (middle); dual mesh (right).

observe qualitatively similar phenomena to Case III (see Fig. 9), that is, the electromagnetic field in the bulk of the domain develops much faster at small λ.

6 Conclusion

We have developed an AP scheme for the Euler-Maxwell plasma model in three spatial dimensions that is applicable in both non-neutral $\lambda = \mathcal{O}(1)$ and quasi-neutral $\lambda \to 0$ regimes. The main features of our work lie in: (i) Maxwell's equations are discretized on primal and dual meshes by FIT (in the spirit of DEC). By discretizing the Euler equations by FVM on the dual mesh, the coupling of two systems is naturally realized via the connection of the mass flux and the electric current at each dual face. (ii) A non-conducting region is taken into account where additional stabilization is essential when $\lambda \to 0$. We enforce the vanishing divergence of the **D**-field through a Lagrange multiplier for any value of λ. (iii) The alignment of primal-dual meshes at the boundary entails cut-off cells and auxiliary unknowns have to be introduced. (iv) A lumping trick is applied to the conductivity matrix (relating the electric current and the electric field) to enhance stability.

Our approach has been tested on a cylindrical domain with settings meant for electric arc simulations. The AP property has been verified numerically. To the best of the authors' knowledge, this work is among the first to try to solve the 3D fluid plasma model on unstructured meshes, which potentially gives more flexibility than the finite-difference-based approaches and reduces the computational cost compared to particle-based approaches. In particular, the AP property allows us to address regimes with vastly different Debye lengths.

References

[1] N. B. Abdallah and P. Degond. On a hierarchy of macroscopic models for semiconductors. *Journal of Mathematical Physics*, 37(7):3306–3333, 07 1996. doi: 10.1063/1.531567.

[2] M. Bessemoulin-Chatard, C. Chainais-Hillairet, and M.-H. Vignal. Study of a finite volume scheme for

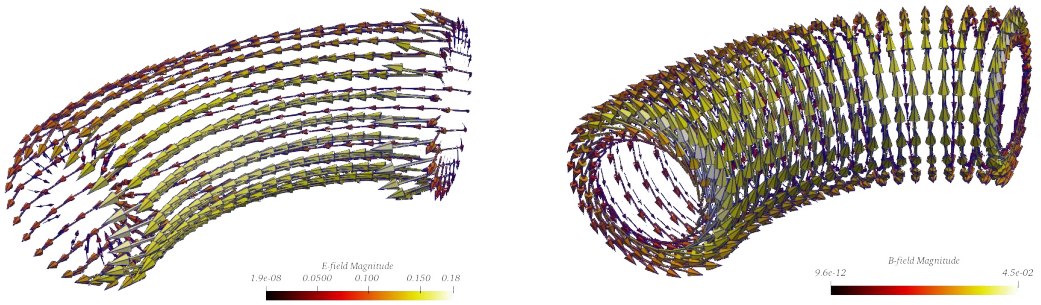

(a) $\lambda = 1$

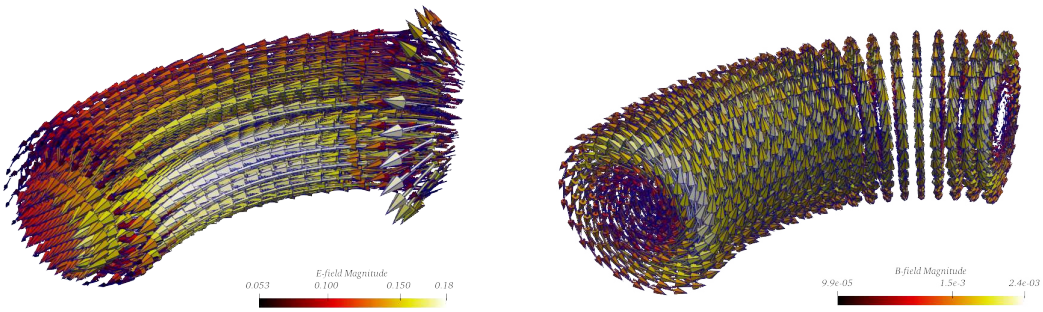

(b) $\lambda = 0$

Fig. 13. Case IV: Snapshots of the **E**-field and **B**-field for different λ at $t = 0.05$.

the drift-diffusion system. Asymptotic behavior in the quasi-neutral limit. *SIAM Journal on Numerical Analysis*, 52(4):1666–1691, 2014. doi: 10.1137/130913432.

[3] S. Bianchini and A. Bressan. Vanishing viscosity solutions of nonlinear hyperbolic systems. *Annals of Mathematics*, 161(1):223–342, 2005.

[4] R. D. Blandford and K. S. Thorne. *Applications of Classical Physics*. California Institute of Technology, 2013.

[5] C. Chainais-Hillairet and F. Filbet. Asymptotic behaviour of a finite-volume scheme for the transient drift-diffusion model. *IMA Journal of Numerical Analysis*, 27(4):689–716, 02 2007. doi: 10.1093/imanum/drl045.

[6] F. Chen. *Introduction to Plasma Physics and Controlled Fusion*. Springer Cham, 3 edition, 01 2016. doi: 10.1007/978-3-319-22309-4.

[7] G.-Q. Chen, J. W. Jerome, and D. Wang. Compressible Euler-Maxwell equations. *Transport Theory and Statistical Physics*, 29(3-5):311–331, 2000. doi: 10.1080/00411450008205877.

[8] W. Chen, K. Wu, and T. Xiong. High order asymptotic preserving finite difference WENO schemes with constrained transport for MHD equations in all sonic mach numbers. *Journal of Computational Physics*, 488:112240, 2023. doi: 10.1016/j.jcp.2023.112240.

[9] P. Degond and F. Deluzet. Asymptotic-preserving methods and multiscale models for plasma physics. *Journal of Computational Physics*, 336:429–457, 2017. doi: 10.1016/j.jcp.2017.02.009.

[10] P. Degond, S. Jin, and J.-g. Liu. Mach-number uniform asymptotic-preserving gauge schemes for compressible flows. *Bull. Inst. Math. Acad. Sin. (N.S.)*, 2, 01 2007.

[11] P. Degond, F. Deluzet, and D. Savelief. Numerical approximation of the Euler-Maxwell model in the quasineutral limit. *Journal of Computational Physics*, 231(4):1917–1946, 2012. doi: 10.1016/j.jcp.2011.11.011.

[12] S. Fabre. Stability analysis of the Euler-Poisson equations. *Journal of Computational Physics*, 101: 445–451, 08 1992. doi: 10.1016/0021-9991(92)90020-Y.

[13] D. Frank-Kamenetskii. *Plasma: The Fourth State of Matter*. Springer New York, NY, 01 1972. doi: 10.1007/978-1-4684-1896-5.

[14] F. Fuchs, S. Mishra, and N. Risebro. Splitting based finite volume schemes for ideal MHD equations. *Journal of Computational Physics*, 228(3):641–660, 2009. doi: 10.1016/j.jcp.2008.09.027.

[15] R. Fuchs. *Numerical Modeling and Simulation of Electric Arcs*. PhD thesis, ETH Zürich, 2021.

[16] P. Gibbon. Introduction to plasma physics, 2020. arXiv:2007.04783.

[17] A. Gleizes, J. J. Gonzalez, and P. Freton. Thermal plasma modelling. *Journal of Physics D: Applied Physics*, 38(9):R153, apr 2005. doi: 10.1088/0022-3727/38/9/R01.

[18] V. Godyak and N. Sternberg. Smooth plasma-sheath transition in a hydrodynamic model. *IEEE Transactions on Plasma Science*, 18(1):159–168, 1990. doi: 10.1109/27.45519.

[19] J. Haack, S. Jin, and J.-g. Liu. An all-speed asymptotic-preserving method for the isentropic Euler and Navier-Stokes equations. *Communications in Computational Physics*, 12, 10 2010. doi: 10.4208/cicp.250910.131011a.

[20] E. Heyn. Asymptotic analysis of singular perturbations. *Zeitschrift für Angewandte Mathematik und Mechanik*, 60(12):740–740, 1980. doi: 10.1002/zamm.19800601217.

[21] R. Hiptmair. Discrete Hodge operators. *Numerische Mathematik*, 90, 11 1999. doi: 10.1007/s002110100295.

[22] R. Hiptmair and J. Ostrowski. Electromagnetic port boundary conditions: Topological and variational perspective. *International Journal of Numerical Modelling: Electronic Networks, Devices and Fields*, 34 (3):e2839, 2021. doi: 10.1002/jnm.2839.

[23] R. Hiptmair and C. Pagliantini. Splitting-based structure preserving discretizations for magnetohydrodynamics. *SMAI Journal of Computational Mathematics*, 4:225–257, 05 2018. doi: 10.5802/smai-jcm.34.

[24] M. Holmes. *Introduction to Perturbation Methods*, volume 20. Springer New York, NY, 01 1995. doi: 10.1007/978-1-4614-5477-9.

[25] K. Hu, Y. Ma, and J. Xu. Stable finite element methods preserving $\nabla \cdot B = 0$ exactly for MHD models. *Numerische Mathematik*, 135(2):371–396, 2017. doi: 10.1007/s00211-016-0803-4.

[26] S. Jin. Efficient asymptotic-preserving (AP) schemes for some multiscale kinetic equations. *SIAM Journal on Scientific Computing*, 21(2):441–454, 1999. doi: 10.1137/S1064827598334599.

[27] S. Jin. Asymptotic preserving (AP) schemes for multiscale kinetic and hyperbolic equations: a review. *Rivista di Matematica della Università di Parma. New Series*, 3, 01 2010.

[28] T. Kato. Remarks on zero viscosity limit for nonstationary Navier-Stokes flows with boundary. In S. S. Chern, editor, *Seminar on Nonlinear Partial Differential Equations*, pages 85–98, New York, NY, 1984. Springer New York.

[29] S. Klainerman and A. Majda. Singular limits of quasilinear hyperbolic systems with large parameters and the incompressible limit of compressible fluids. *Communications on Pure and Applied Mathematics*, 34(4):481–524, 1981. doi: 10.1002/cpa.3160340405.

[30] H. Kumar and S. Mishra. Entropy stable numerical schemes for two-fluid plasma equations. *Journal of Scientific Computing*, 52, 11 2011. doi: 10.1007/s10915-011-9554-7.

[31] R. J. LeVeque. *Finite Volume Methods for Hyperbolic Problems*. Cambridge Texts in Applied Mathematics. Cambridge University Press, 2002. doi: 10.1017/CBO9780511791253.

[32] R. J. LeVeque. *Finite Difference Methods for Ordinary and Partial Differential Equations*. Society for Industrial and Applied Mathematics, 2007. doi: 10.1137/1.9780898717839.

[33] Y. Li, Y.-J. Peng, and L. Zhao. Convergence rates in zero-relaxation limits for Euler-Maxwell and Euler-Poisson systems. *Journal de Mathématiques Pures et Appliquées*, 154:185–211, 2021. doi: 10.1016/j.matpur.2021.08.011.

[34] J. Liu and L. Wu. Fast-converging and asymptotic-preserving simulation of frequency domain thermoreflectance. *Communications in Computational Physics*, 05 2023. doi: 10.4208/cicp.OA-2023-0053.

[35] n. M. Bonotto, n. D. Abate, n. P. Bettini, and F. Villone. A Coupled FEM-BEM Approach for the Solution of the Free-Boundary Axi-Symmetric Plasma Equilibrium Problem. *Communications in Computational Physics*, 31(1):27–59, June 2022. doi: 10.4208/cicp.OA-2021-0062.

[36] M. Marrone. Computational aspects of the cell method in electrodynamics. In F. Teixeira, editor, *Geometric Methods for Computational Electromagnetics*, volume 32 of *PIER*, pages 317–356. EMW Publishing, Cambridge, MA, 2001.

[37] R. Methling, N. Götte, and D. Uhrlandt. Ablation-dominated arcs in CO2 atmosphere—part ii: Molecule emission and absorption. *Energies*, 13(18), 2020. doi: 10.3390/en13184720.

[38] S. Parker, R. Procassini, C. Birdsall, and B. Cohen. A suitable boundary condition for bounded plasma simulation without sheath resolution. *Journal of Computational Physics*, 104(1):41–49, 1993. doi: 10.1006/jcph.1993.1005.

[39] Y.-J. Peng and S. Wang. Rigorous derivation of incompressible e-MHD equations from compressible Euler–Maxwell equations. *SIAM Journal on Mathematical Analysis*, 40(2):540–565, 2008. doi: 10.1137/070686056.

[40] Y.-J. Peng, S. Wang, and Q. Gu. Relaxation limit and global existence of smooth solutions of compressible Euler–Maxwell equations. *SIAM Journal on Mathematical Analysis*, 43(2):944–970, 2011. doi: 10.1137/100786927.

[41] B. Perot. Conservation properties of unstructured staggered mesh schemes. *Journal of Computational Physics*, 159(1):58–89, 2000. doi: 10.1006/jcph.2000.6424.

[42] A. Rodríguez and A. Valli. *Eddy Current Approximation of Maxwell Equations: Theory, Algorithms and Applications*, volume 4. Springer Milano, 01 2010. doi: 10.1007/978-88-470-1506-7.

[43] L. Saint-Raymond. *Hydrodynamic Limits of the Boltzmann Equation*. Springer Berlin, Heidelberg, 03 2009. doi: 10.1007/978-3-540-92847-8.

[44] M. Seeger. Perspectives on research on high voltage gas circuit breakers. *Plasma Chemistry and Plasma Processing*, 35(3):527–541, 2015. doi: 10.1007/s11090-014-9595-4.

[45] R. Sentis. *Mathematical Models and Methods for Plasma Physics. Volume 1. Fluid models*. Birkhäuser Cham, 01 2014. doi: 10.1007/978-3-319-03804-9.

[46] T. Tarhasaari, L. Kettunen, and A. Bossavit. Some realizations of a discrete Hodge operator: A reinterpretation of finite element techniques [for EM field analysis]. *IEEE Transactions on Magnetics*, 35(3):1494–1497, 1999. doi: 10.1109/20.767250.

[47] F. L. Teixeira and W. C. Chew. Lattice electromagnetic theory from a topological viewpoint. *Journal of Mathematical Physics*, 40(1):169–187, 1999. doi: 10.1063/1.532767.

[48] R. Temam and X. Wang. On the behavior of the solutions of the Navier-Stokes equations at vanishing viscosity. *Annali della Scuola Normale Superiore di Pisa - Classe di Scienze*, Ser. 4, 25(3-4):807–828, 1997.

[49] E. Tonti. Finite formulation of electromagnetic field. *IEEE Transactions on Magnetics*, 38(2):333–336, 2002. doi: 10.1109/20.996090.

[50] V. Wasiolek. Uniform global existence and convergence of Euler-Maxwell systems with small parameters. *Communications on Pure and Applied Analysis*, 15(6):2007–2021, 2016. doi: 10.3934/cpaa.2016025.

[51] T. Weiland. A discretization model for the solution of Maxwell's equations for six-component fields. *Archiv Elektronik und Uebertragungstechnik*, 31:116–120, Apr. 1977.

[52] T. Weiland. Finite integration method and discrete electromagnetism. In *Computational Electromagnetics*, pages 183–198, Berlin, Heidelberg, 2003. Springer Berlin Heidelberg.

[53] K. Wu. Positivity-preserving analysis of numerical schemes for ideal magnetohydrodynamics. *SIAM Journal on Numerical Analysis*, 56(4):2124–2147, 2018. doi: 10.1137/18M1168017.

[54] K. Wu and C.-W. Shu. Geometric quasilinearization framework for analysis and design of bound-preserving schemes. *SIAM Review*, 65(4):1031–1073, 2023. doi: 10.1137/21M1458247.

[55] K. Wu, H. Jiang, and C.-W. Shu. Provably positive central discontinuous Galerkin schemes via geometric quasilinearization for ideal MHD equations. *SIAM Journal on Numerical Analysis*, 61(1):250–285, 2023. doi: 10.1137/22M1486996.

[56] K. Yee. Numerical solution of initial boundary value problems involving Maxwell's equations in isotropic media. *IEEE Transactions on Antennas and Propagation*, 14(3):302–307, 1966. doi: 10.1109/TAP.1966.1138693.